Development of Optical Nanoprobes for Molecular Imaging of Reactive Oxygen and Nitrogen Species

Xu Zhen and Kanyi Pu*

School of Chemical and Biomedical Engineering, Nanyang Technological University, Singapore 637457, Singapore

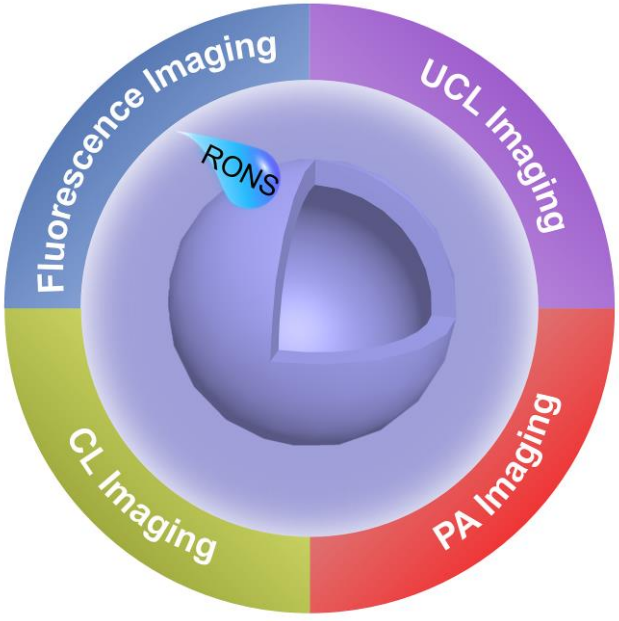

This review summarizes the development of optical nanoprobes with near-infrared (NIR) fluorescent, upconversion luminescent (UCL), chemiluminescent (CL), or photoacoustic (PA) signals for molecular imaging of RONS in living systems.

Author 1-2, http://www.ntu.edu.sg/home/kypu/index.html

Development of Optical Nanoprobes for Molecular Imaging of Reactive Oxygen and Nitrogen Species

Xu Zhen and Kanyi Pu (✉)

School of Chemical and Biomedical Engineering, Nanyang Technological University, Singapore 637457, Singapore

Received: day month year
Revised: day month year
Accepted: day month year (automatically inserted by the publisher)

KEYWORDS

optical imaging, reactive oxygen and nitrogen species, fluorescent, upconversion luminescence, chemiluminescence, photoacoustic imaging

ABSTRACT

Reactive oxygen and nitrogen species (RONS) play important roles in cell signal transduction, while overproduction of RONS may disrupt cellular homeostasis, causing oxidative and nitrosative stresses and associated with a series of pathological processes. Therefore, accurate methods to selectively and specifically monitor RONS in living systems are required to further elucidate their biological functions. Optical imaging has the advantages of the prominent sensitivity, high spatiotemporal resolution, and real-time imaging capability, showing great potential for the detection of RONS in living systems. This review summarizes the development of optical nanoprobes with near-infrared (NIR) fluorescent, upconversion luminescent, chemiluminescent, or photoacoustic signals for molecular imaging of RONS in living systems. The design principles of RONS-responsive activatable nanoprobes and the advantages of these optical imaging modalities are discussed along with their imaging applications in different diseases models.

1 Introduction

Reactive oxygen and nitrogen species (RONS) including superoxide anion radicals ($O_2^{\cdot-}$), hydrogen peroxide (H_2O_2), hypochlorite (ClO^-), hydroxyl radicals (·OH) and peroxynitrite ($ONOO^-$) produced in living systems play critical roles in a variety of physiological and pathological processes including cell signal transduction, inflammation, cancer, cardiovascular diseases, arthritis, diabetes, and neurodegenerative diseases [1-3]. As shown in Figure 1, $O_2^{\cdot-}$, a primary ROS, can be formed by a one-electron transfer to oxygen from the action of nicotinamide adenine dinucleotide phosphate-oxidase [NADPH] oxidases in the plasma membranes or various organelles such as mitochondria, phagosomes, and

Address correspondence to Kanyi Pu, kypu@ntu.edu.sg

chloroplasts [4, 5]. $O_2^{\cdot-}$ can be catalyzed by superoxide dismutase (SOD) to produce H_2O_2 [6]. In the presence of iron ion catalyst, ·OH can be generated from $O_2^{\cdot-}$ and H_2O_2 through Fenton reaction [7]. HOCl can be generated through an oxidation reaction between H_2O_2 and chloride ions under the catalysis of myeloperoxidase (MPO) [8]. $ONOO^-$ is formed through the reaction between $O_2^{\cdot-}$ and nitric oxide [9]. Although RONS can act as signaling molecules under normal physiological processes, overproduction of RONS induces oxidative and nitrosative stresses *via* DNA, lipids, proteins, and carbohydrates oxidation [10-16].

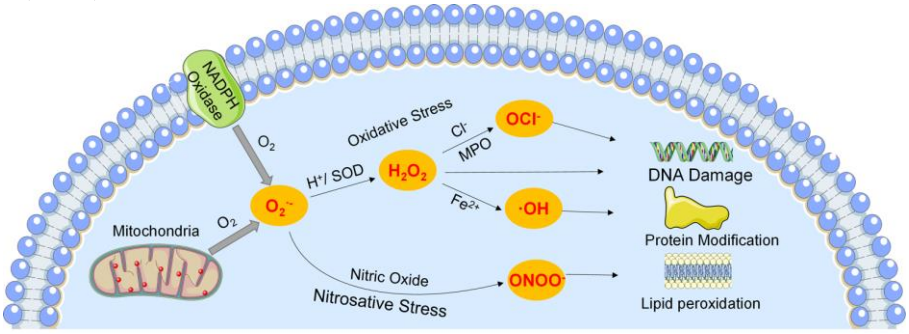

Figure 1. Schematic diagram of the generation of RONS and the potential hazard of the overproduction of RONS in living organisms.

Development of accurate and sensitive analytical tools for selective monitoring of RONS in living systems is significant to elucidate their biological functions [17-22]. However, the low actual concentration and high reactivity of RONS in living systems make this imaging task very challenging. Optical imaging using non-ionizing radiation including ultraviolet, visible, and near-infrared (NIR) light, significantly decreases the risk of patients to the harmful radiation used in other imaging techniques such as computed tomography (CT) and positron emission tomography (PET). Moreover, optical imaging has the distinguished advantages of prominent sensitivity, high spatial and temporal resolution, and real-time imaging capability. In the past several decades, small molecule-based probes have been developed for optical imaging of RONS, and a number of nice reviews have been published [23-28]. Some small molecule based RONS probes have been commercialized [29]. These probes have the advantages of small sizes, fast response and easy functionalization, which are useful for cell staining and ex vivo sensing. However, most of these small molecule probes have the general issues of poor water-solubility, fast photobleaching, and lack of targeting ability to the disease sites; moreover, a few can emit signals in the near-infrared (NIR) region, limiting their capability for in vivo imaging. Compared with small molecule probes, nanoprobes can have improved water-solubility and good photostability, high payload capacity for multiplexing and multimodal imaging, and prolonged blood circulation time to accumulate in the disease sites [30-37]. Synthetic versatility of optical nanoprobes also allows them to be modified to emit NIR light for in vivo imaging of RONS.

In this Review, we summarize the development of optical nanoprobes with fluorescence, upconversion luminescence (UCL), chemiluminescence (CL), or photoacoustic (PA) imaging capabilities for the detection of RONS in living subjects, such as mice. Chemical structures of the optical agents used for the preparation of nanoprobes including semiconducting polymers (SPs), semiconducting oligomers (SOs), amphiphilic polymers, and small molecular chromophores are summarized in Figure 2. The different imaging approaches for the detection of different RONS are summarized and compared in Table 1. In the following, the in vitro and in vivo

applications of nanoprobes for fluorescence, UCL, CL, and PA imaging are sequentially discussed. The design and optical properties of each nanoprobe are discussed according to the requirement of specific imaging of RONS. At last, the potential challenges and perspectives of optical nanoprobes for the detection of RONS are analyzed.

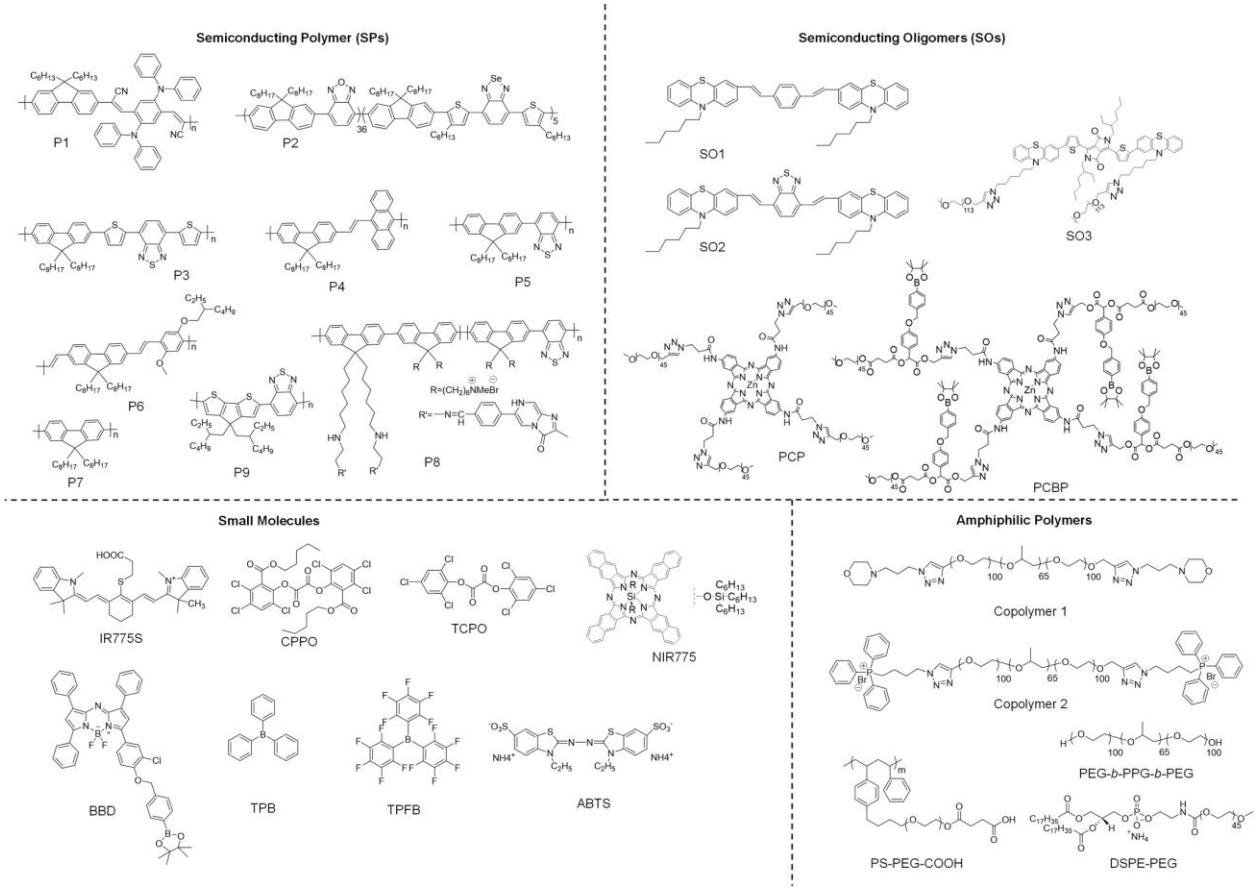

Figure 2. Chemical structures of SPs, SOs, small molecular chromophores, and amphiphilic polymers used for the preparation of optical nanoprobes for RONS imaging.

Table 1. Summary of the imaging approaches for the detection of different RONS.

RONS	Imaging modality	Disease model	Detection approach	Ref.
$O_2^{\cdot-}$	CL	LPS-induced acute inflammation and tumor	Turn on	[83]
H_2O_2	CL	LPS-induced peritoneal inflammation	Turn on	[75]
	CL	LPS-induced arthritis	Turn on	[74]
	CL	Drug-induced hepatotoxicity	Turn on	[77]
	CL	LPS-induced peritonitis and neuro-inflammation	Turn on	[78]
	PA	LPS-induced inflammation	Turn on	[108]

		and tumor		
	PA	Tumor	Turn on	[109]
ClO^-	Fluorescence	*Corynebacterium bovis (C. bovis)* bacterial infection	Ratiometric	[49]
	Fluorescence	LPS-induced peritonitis	Ratiometric	[50]
	PA	Tumor	Ratiometric	[106]
·OH	UCL	LPS-induced liver inflammation	Turn on	[70]
$ONOO^-$	Fluorescence	*Corynebacterium bovis (C. bovis)* bacterial infection	Ratiometric	[49]
	PA	Tumor	Ratiometric	[107]
	PA	Tumor	Turn on	[109]
	UCL	Drug-induced hepatotoxicity	Turn on	[71]

2 Fluorescence imaging

Real-time fluorescence imaging of chemical species in live organisms requires nanoprobes to possess bright fluorescence, low cytotoxicity and excellent photostability. Quantum dots (QDs)[38], polymer nanoparticles [39-41], gold nanoparticles [42], silica nanoparticles [43], and carbon dots [44] have been used for in vitro and in vivo fluorescence imaging. However, smart activatable nanoprobes with specific fluorescence responses toward RONS have been rarely reported [45-48].

Taking advantage of the RONS-inert property of SPs, a NIR fluorescence ratiometric nanoprobe based on SP nanoparticles (SPNs) was developed for detection of RONS in vivo. This nanoprobe (SPN-P1) was composed of poly[9,90-dihexyl-2,7-bis(1-cyanovinylene) fluorenylenealt-co-2,5-bis(N,N-diphenylamino)-1,4-p-he-nylene] (P1) and a RONS sensitive cyanine dye derivative (IR775S) [49]. IR775S was conjugated with nanoparticle through a carbodiimide coupling reaction to obtain the nanoprobe (SPN-P1) (Figure 3a). Due to FRET, SPN-P1 exhibited a dual emission peak at 678 (P1) and 818 nm (IR775S) upon excitation (Figure 3a&b). In the presence of RONS, IR775S was rapid oxidative cleaved and subsequently the FRET process within SPN-P1 was disturbed, resulting in the ratiometric fluorescence activation towards RONS. Taking $ONOO^-$ as an example, the emission peak of SPN-P1 at 678 nm gradually increased with the concomitant decrease of emission at 808 nm upon addition of $ONOO^-$ (Figure 3b). Besides $ONOO^-$, the nanoprobe can be activated by ClO^- and ·OH but not by H_2O_2 and other RONS (Figure 3c). SPN-P1 was then utilized for detection of RONS in mice models of spontaneous *Corynebacterium bovis (C. bovis)* bacterial infection. After intravenous injection of SPN-P1 to mice, SPN-P1 was first accumulated in the infected site within 15 minutes due to the enhanced permeability and retention (EPR) effect, and then the probe was gradually activated by RONS produced in the infection areas, with nearly complete probe activation by 60 minutes (Figure 3d&e).

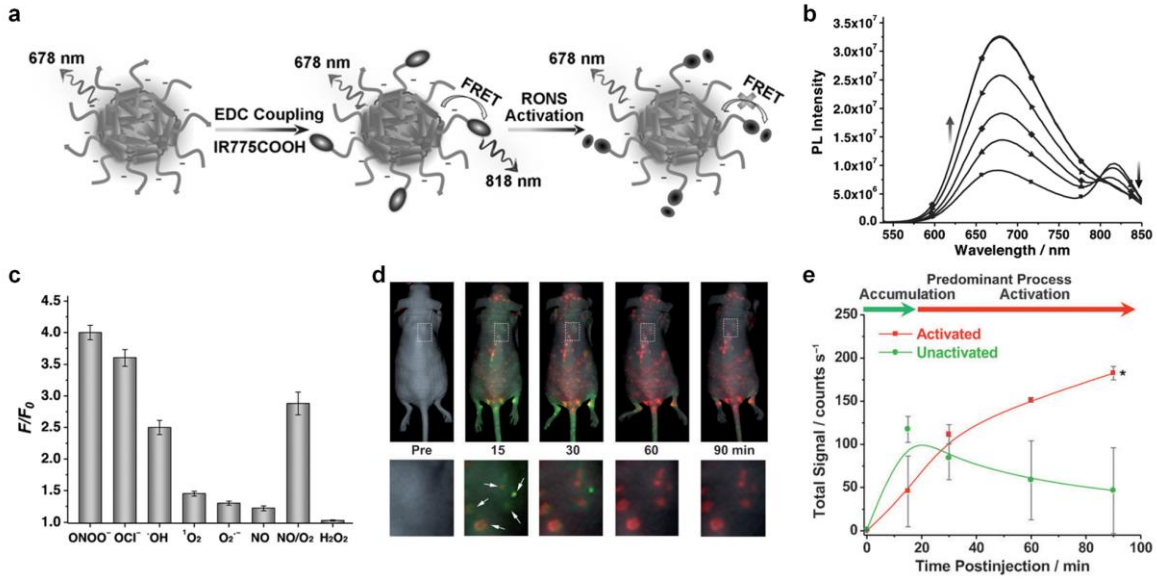

Figure 3. (a) Preparation and RONS sensing mechanism of SPN-P1. (b) Fluorescence spectra of SPN-P1 in PBS (pH = 7.4) in the absence or presence of different concentrations $ONOO^-$ (0.1, 0.2, 0.3, 0.4, or 0.5 μM). (c) Fluorescence responses of SPN-P1 (0.1 μg mL^{-1}) toward different RONS in PBS (pH = 7.4). F and F_0 stand for the fluorescence intensities at 678 nm in the presence and absence of RONS (1 μM), respectively. Excitation at 405 nm. (d) Imaging RONS with SPN-P1 in mice with spontaneous systemic C. bovis bacterial infection. Overlaid images of activated (red) and unactivated (green) SPN-P1 following i.v. administration to mice with spontaneous infections (n = 4). Enlargements of the regions indicated by dashed white boxes are given below each corresponding image. White arrows indicate localized regions of bacterial infection. (e) Quantification of activated (red) and nonactivated (green) SPN-P1 fluorescence over time. Reprinted with permission from Ref. [49], copyright 2013, WILEY-VCH Verlag GmbH & Co. KGaA, Weinheim.

Recently, Chiu et al. reported the ratiometric detection of ClO^- in living mice using a SPN-based probe (SPN-P2) [50]. P2 comprised a ClO^--inert component, benzoxadiazole (OBT) as the energy donor and a ClO^--sensitive fluorophore, 4,7-bis(2-thienyl)-2,1,3-benzoselenadiazole (SeTBT) as the energy acceptor, enabling FRET from OBT (540 nm) to SeTBT (680 nm) in the absence of ClO^- (Figure 4a). In the presence of ClO^-, oxidation of SeTBT occurred and subsequently the FRET process within SPN-P2 was abolished, resulting in the increased emission intensity of OBT (540 nm) and the decreased emission of SeTBT (680 nm). SPN-P2 thus could be used for the ratiometric detection of ClO^-. (Figures 4a-c). The fluorescent color of SPN-P2 was initially red, which turned to orange, yellow and finally to green with the increasing concentrations of ClO^- from 0 to 500 μM (Figure 4d). The emission ratio of SPN-P2 barely changed in the presence of other ROS or biologically relevant analytes (Figure 4e), validating its high selectivity towards ClO^-. Thus, SPN-P2 was suitable for the detection of exogenous ClO^- in living mice (Figure 4f) and endogenous ClO^- in a model for lipopolysaccharide (LPS)-induced peritonitis in living mice (Figure 4g).

Address correspondence to Kanyi Pu, kypu@ntu.edu.sg

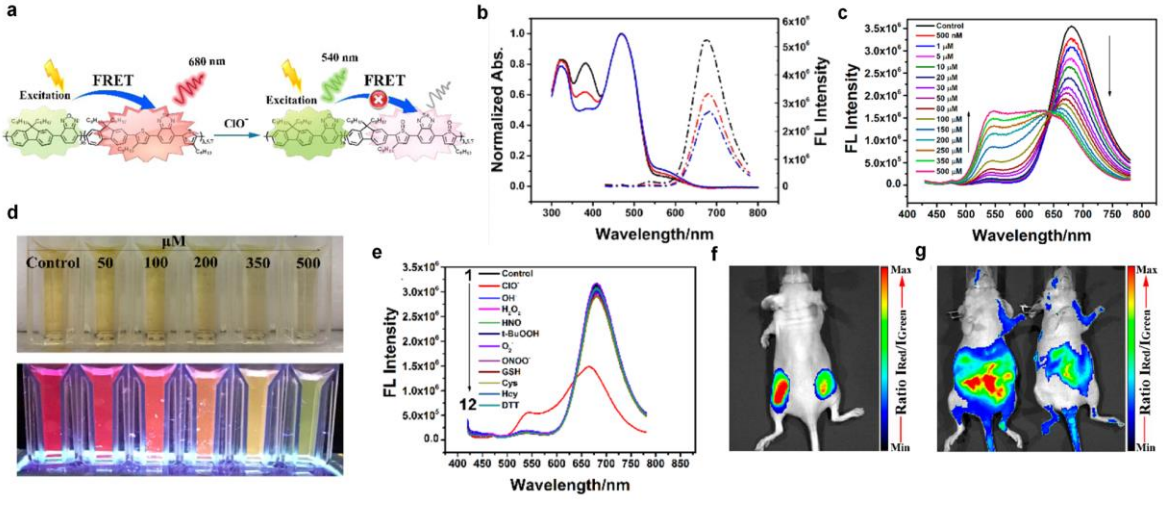

Figure 4. (a) Schematic illustration of SPN-P2 for ClO^- sensing. (b) Normalized absorption (solid line) and emission (dashed line) spectra of SPN-P2. (c) Fluorescence performance of SPN-P2 in the presence of different concentrations of ClO^-. (d) Photographs of SPN-P2 in the presence of different concentrations of ClO^- taken under normal laboratory lighting and illumination with a UV light at 365 nm. (e) Fluorescence spectra of SPN-P2 in the presence of various ROS and biologically relevant analytes. (f) In vivo imaging of exogenous ClO^- using SPN-P2. Representative ratiometric (pseudocolor) image of mice with the subcutaneous implantation of SPN-P2 (left) and SPN-P2 + ClO^- (right). (g) In vivo imaging of endogenous ClO^- production from the peritoneal cavity of the mice with SPN-P2 during an LPS-mediated inflammatory response. Representative ratiometric images (pseudocolor) of mice intraperitoneally treated with saline (left) and LPS (right), followed by an intraperitoneal injection of SPN-P2 4 h later. Fluorescence images were acquired 30 min after the injection of SPN-P2 with a 465 nm excitation filter and 540 nm (green channel) and 680 nm (red channel) emission filters. Ratiometric images were obtained by pixel-by-pixel calculation using ImageJ software. Reprinted with permission from Ref. [50]. Copyright 2017, American Chemical Society.

A nanoprobe cocktail approach based on semiconducting oligomer nanoparticles (SONs) was designed for multicolor and multiorganelle imaging of ClO^- in living cells [51]. Two oligomers (SO1&SO2) and two amphiphilic block copolymers (copolymer 1 and copolymer 2) were synthesized. Both oligomers contained phenothiazine unit as ClO^- sensing part but displayed different fluorescent color responses. The copolymers 1 and 2 had morpholine and triphenylphosphine groups to target lysosome and mitochondria, respectively. Co-nanoprecipitation between the SO and the targeting amphiphilic copolymer resulted in the lysosome-targeted nanoprobe (LNP) composed of SO1 and copolymer 1, and the mitochondria-targeted nanoprobe (MNP) composed of SO2 and copolymer 2, respectively. By selective light excitation of each nanoprobe, the LNP/MNP cocktail allowed for simultaneous fluorescence imaging of elevated level of ClO^- in lysosome and mitochondria according to the alteration of fluorescence colors. Under excitation at 405 nm for LNP, the single emission peak at 535 nm was gradually changed to the dual peaks at 472 and 590 nm after activation by ClO^- (Figure 5a). Under excitation at 570 nm for MNP, the emission peak at 690 nm was gradually blue-shifted to 610 nm after activation by ClO^- (Figure 5b). ClO^- triggered a remarkable enhancement of emission ratio I_{472}/I_{535} (λ_{ex} = 405 nm) and I_{610}/I_{690} (λ_{ex} = 570 nm), respectively, while various other RONS including H_2O_2, $ONOO^-$, $O_2^{\cdot-}$, $^1O_2$, and ·OH did not result in any obvious changes (Figure 5c). The nanoprobe cocktail was then used for multilocal and multicolor imaging of elevated ClO^- in murine macrophage cell line (RAW 264.7) treated with

LPS and a dimerized soluble cytokine, interferon-γ (IFN-γ). Strong fluorescence signals were observed for the green (520-550 nm) and red (690-750 nm) channels after incubating the resting macrophage cells (control) or the cells co-treated with LPS/IFN-γ and N-acetyl-L-cysteine (NAC, a ROS scavenger) with the nanoprobe cocktail (Figure 5d). In contrast, strong fluorescence signals were observed for the blue (420-460 nm) and orange (580-610 nm) channels when the RAW 264.7 cells were only pre-stimulated with LPS/IFN-γ, demonstrating that the nanoprobe cocktail was activated by ClO^- in both lysosome and mitochondria of stimulated macrophage cells (Figure 5d). This design verified the potential of the nanoprobe cocktail for multilocal and multicolor fluorescence imaging of ClO^- in living organisms.

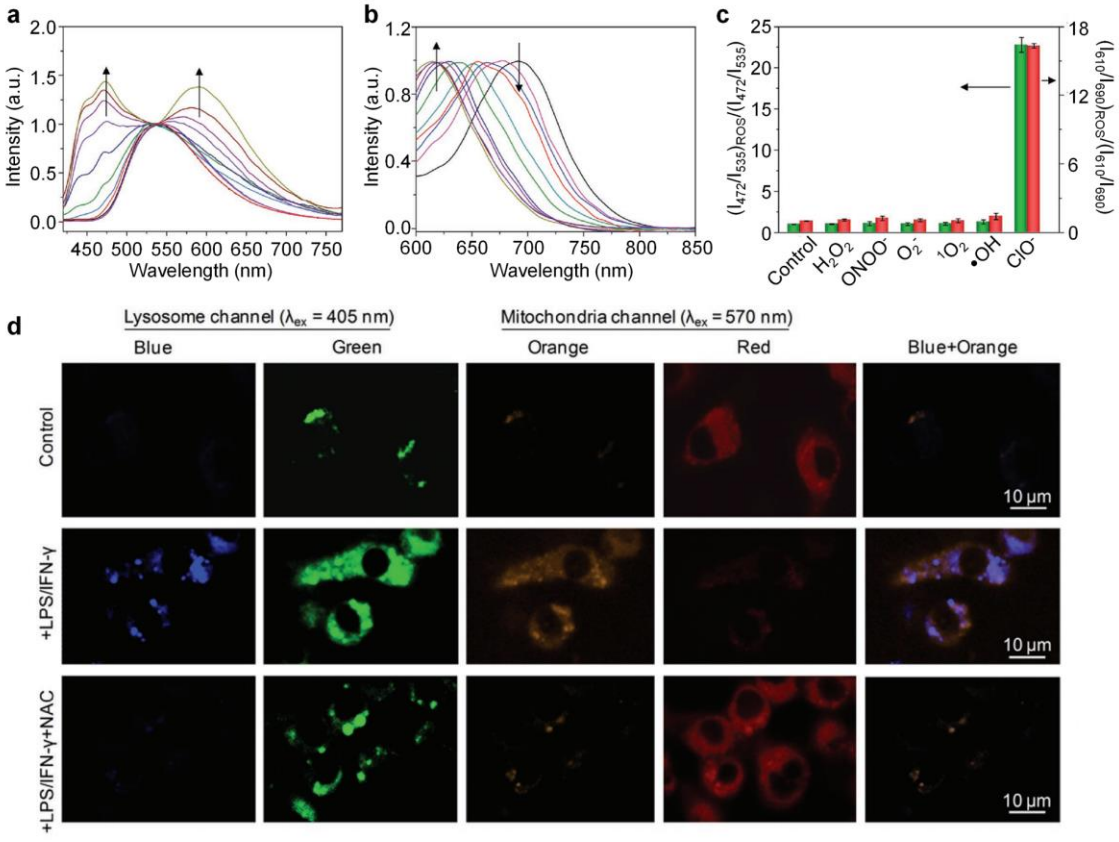

Figure 5. (a) Fluorescence spectra evolution of LNP/MNP cocktail nanoprobe solution upon treatment of ClO^- from 0 to 20 × 10^{-6} M at the interval of 2 × 10^{-6} M. Excitation at 405 nm. (b) Normalized fluorescence spectra of LNP/MNP cocktail nanoprobe solution upon treatment of ClO^- from 0 to 20 × 10^{-6} M at the interval of 2 × 10^{-6} M. Excitation at 507 nm. (c) The ratios of ratiometric fluorescence intensity of the LNP/MNP cocktail nanoprobe (I_{472}/I_{535} and I_{610}/I_{690}) in the presence of ROS to that in the absence of ROS. (d) Multilocal and multicolor imaging of ClO^- in murine macrophage cells (RAW 264.7). Control: RAW 264.7 cells were incubated with the nanoprobe for 24 h without any pretreatment. +LPS/IFN-γ: Cells were pretreated with LPS/IFN-γ for 24 h and then incubated with the nanoprobe for another 24 h. +LPS/IFN-γ + NAC: Cells were pretreated with LPS/IFN-γ and NAC for 24 h and then incubated with the nanoprobe for another 24 h. All the imaging signals were collected through four channels: blue (420–460 nm, λ_{ex} = 405 nm), green (520–550 nm, λ_{ex} = 405 nm), orange (580–610 nm, λ_{ex} = 570 nm), and red (690–750 nm, λ_{ex} = 570 nm). Reprinted with permission from Ref. [51]. Copyright 2017, WILEY-VCH Verlag GmbH & Co. KGaA, Weinheim.

In addition to organic nanoparticles, inorganic nanoparticles, such as graphene quantum dots (QDs) [52], carbon dots [53], silver nanoclusters (AgNCs) [54] and gold nanoclusters (AuNCs) [55], could be used for

imaging of RONS. For instance, Lu et al. reported that the fluorescence of the AuNCs could be quenched by RONS, including ClO^-, $ONOO^-$, and ·OH [56]. Accordingly, a dual-emission fluorescent nanocomplex (DEFN) based on AuNCs and a RONS-inert dye encapsulated core silica nanoparticles were designed for highly RONS (hRONS) imaging in living cells. The AuNCs was conjugated to the surface of silica nanoparticles to obtain DEFN. DEFN showed a single-excitation (405 nm), two different emission fluorescence peaks, corresponded to the decorated AuNCs (565 nm) and the dye-encapsulated silica nanoparticles (435 nm), respectively. With the increasing concentration of hRONS, the fluorescence intensity at 565 nm from the AuNCs decreased gradually, while the fluorescence intensity at 435 nm assigned to the encapsulated dye barely changed. A good linear relationship between the ratiometric fluorescence signal (I_{435}/I_{565}) and the hRONS concentrations was detected, demonstrating that DEFN had the potential for quantification of hRONS. The live cell imaging with three different cell lines including HeLa cells, HL-60 cells, and RAW 264.7 cells showed DEFN allowed sensitive and rapid imaging of hRONS in living cells.

3 Upconversion luminescence (UCL) imaging

The tissue autofluorescence generated from real-time light excitation can interfere with sensing signal and thus compromise detection sensitivity. Moreover, the short excitation wavelengths in UV or visible range leads to shallow tissue penetration depths. In contrast to fluorescence, UCL is a non-linear optical, anti-stokes process that converts two or more low-energy excitation photons from the NIR region to higher energy emission photons with a shorter wavelength [57, 58]. Recently, upconversion nanoparticles (UCNPs) containing rare-earth elements have been exploited for applications in bioimaging and biosensing [59-63]. Compared to conventional fluorescent probes, UCNPs offer the enhanced photostability and thermal stability. Moreover, UCNPs show anti-Stokes emission upon low levels of irradiation in the NIR region that is within the optical transparency window. Therefore, the NIR excitation of UCNPs also offers a higher tissue penetration depth (up to 10 mm) and much lower scattering and autofluorescence backgrounds as compared to visible wavelengths, leading to improved signal-to-noise ratios [64-66]. In addition, UCNPs also show a sharp emission bandwidth, long lifetime and tunable emission, which benefit the bioimaging application [59]. In order to endow them with in vivo RONS biosensing applications, the UCNPs core could act as an energy donor and the sensing moiety could be an energy acceptor to achieve RONS-triggered luminescence resonance energy transfer (LRET) [67]. Following this LRET principle, UCNPs have been exploited for RONS imaging [68].

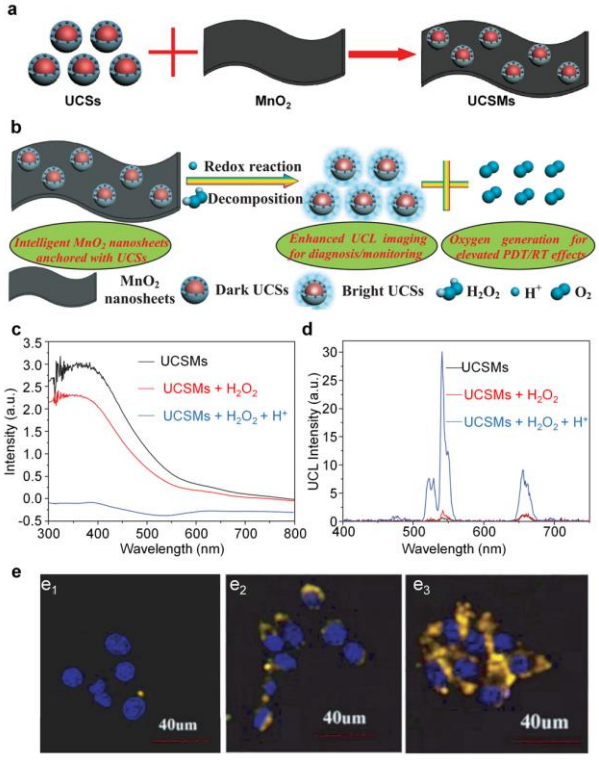

Figure 6. (a) Schematic illumination of the construction of MnO_2 nanosheets anchored with upconversion nanoprobes (UCSMs). (b) Schematic illustration of the decomposition of MnO_2 nanosheets through the redox reaction between UCSMs and acidic H_2O_2. (c) The UV-vis absorption spectrum and (d) UCL emission spectrum

of UCSMs, UCSMs with H_2O_2 in neutral environment (pH = 7.4), and UCSMs with H_2O_2 in acid environment (pH = 5.5). (e) Confocal laser scanning microscopy (CLSM) images of hc-4T1 cells after incubation with UCSMs for e_1) 1 h, e_2) 8 h, and e_3) 20 h, respectively. Reprinted with permission from Ref. [69]. Copyright 2015, WILEY-VCH Verlag GmbH & Co. KGaA, Weinheim.

Recently, Shi group reported a novel 2D theranostic nanomaterial that utilized manganese oxide (MnO_2) nanosheets to engineer upconversion nanoprobes (UCSM) for highly sensitive UCL imaging of H_2O_2 in tumors and oxygen-elevated synergetic therapy [69]. A photosensitizer-incorporated dense silica shell was coated on the surface of UCNPs ($NaYF_4$:Yb/Er/Tm) to form the theranostic upconversion nanoprobes (UCSs); then MnO_2 nanosheets were anchored to the surface of UCSs to obtain the final UCSMs (Figure 6a). MnO_2 showed a broad absorption spectrum overlapping the emission of UCSs, which enabled energy transfer from UCSs to MnO_2 and resulted in significant quenching of UCL (Figure 6b). In a neutral environment of H_2O_2, the quenched UCL of UCSMs was hardly recovered because the MnO_2 only acted as a catalyst but not reduced itself (Figure 6c&d). However, in the acid environment of H_2O_2 (pH = 5.5), the quenched UCL of UCSMs could be recovered through the decomposition of MnO_2 into colorless Mn^{2+}, while H_2O_2 was oxidized to O_2, leading to the enhancement in UCL signal and the massive oxygen generation for the synergetic therapy (Figure 6b&c&d). Therefore, this UCSMs were used as an effective biosensor for UCL imaging of hypoxic murine breast cancer cells, which could detect the concentrations of endogenous acidic H_2O_2. Much stronger yellow luminescence could be observed in the hypoxic cells with the increased incubation time from 1 h (Figure 6e_1) to 8 (Figure 6e_2) and 20 h (Figure 6e_3), demonstrating that more and more UCSMs were uptaken into the cells and the UCL was significantly recovered due to the decomposition of MnO_2 in the cells. This design verified the potential of UCNPs for the concurrent stimuli-responsive imaging of acid H_2O_2 in living organisms.

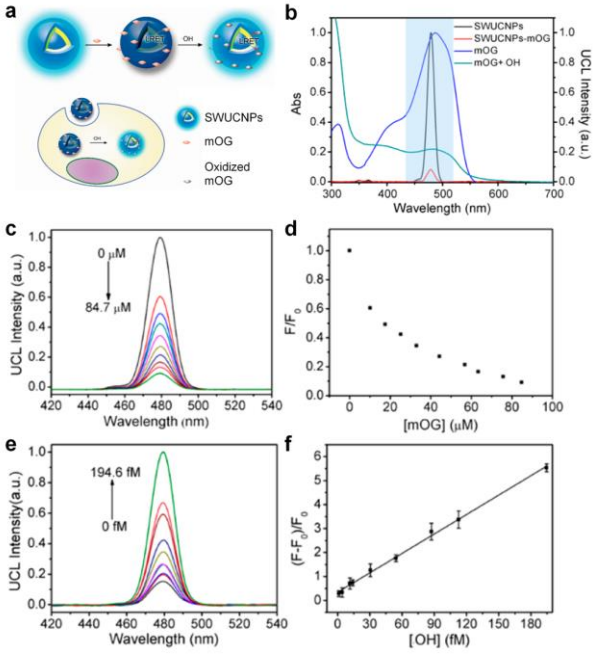

Figure 7. (a) Schematic illumination of the UCNPs for ·OH detection. (b) The emission spectrum of SWUCNPs and SWUCNPs-mOG. The absorption spectrum of mOG and mOG with ·OH. (c) The emission spectrum of SWUCNPs loaded with different concentrations of mOG. (d) Relative fluorescence intensity (F and F_0 represent the UCL emission intensity in the presence and the absence of mOG, respectively) of SWUCNPs after assembly of different concentrations of mOG. (e) UCL emission spectrum of mOG-SWUCNPs with different concentrations of ·OH. (f) Relative fluorescence intensity of the mOG-SWUCNPs in response to different concentrations of ·OH. Reprinted with permission from Ref. [70]. Copyright 2015, American Chemical Society.

Liu et al. reported a dye-coated UCNP for in vivo imaging of ·OH. This nanoprobe had sandwich structured UCNPs (SWUCNPs, $NaYF_4$@$NaYF_4$:Yb,Tm@$NaYF_4$) as the energy donors and an ·OH sensitive azo dye (mOG) as the energy acceptor[70]. The carboxyl groups of mOG coordinated with the lanthanide ions on the surface of the SWUCNPs to form the mOG-SWUCNPs. Due to the well overlap between absorption of mOG and

emission of SWUCNPs, LRET occurred and UCL was quenched by mOG (Figure 7a&b). In the presence of ·OH, mOG was rapidly oxidized and decomposed, and thus the LRET process within the moG-SWUCNPs was disturbed, leading to the recovery of UCL of SWUCNPs (Figure 7a). The UCL of SWUCNPs was gradually decreased with the increasing concentrations of mOG (Figure 7c). 90% UCL of SWUCNPs was quenched by mOG, when 84.7 μM mOG was loaded on 1.2 mg/mL SWUCNPs (Figure 7d). With increasing amounts of $NaNO_3$, the UCL of SWUCNPs was gradually recovered (Figure 7e). The relative UCL intensity had an excellent linear relationship with the concentration of ·OH in the range from 1.2 to 194.6 fM (Figure 7f). The detection limit of mOG-SWUCNPs for ·OH was determined to be 1.2 fM, several orders of magnitude lower than other reported fluorescence probes for ·OH. This nanoprobe could be used for in vivo detection of ·OH in an LPS model of acute inflammation in living mice.

Such a dye-coated design also made UCNPs useful for in vivo imaging of drug-induced hepatotoxicity in living mice. Chang and Liu's groups developed a core-shell lanthanide-doped UCNPs coated with polyethyleneimine (PEI) and cyanine (Cy7) for monitoring Acetaminophen (APAP)-induced drug hepatotoxicity in living mice (Figure 8a) [71]. APAP is an antipyretic analgesic drug. Overdose of APAP could cause acute hepatotoxicity through oxidative and nitrosative stress to generate RONS. The UCNPs were set as energy donor and the RNS-responsive Cy7 was used as energy acceptor. Note that Cy7 dye had the similar structure to IR775S discussed in the fluorescence section, which could be rapidly oxidized by $ONOO^-$ or ClO^-. The emission of UCNPs matched well with the absorption of Cy7, leading to LRET from UCNPs to Cy7 and in turn quenched UCL (Figure 8b). In the presence of $ONOO^-$, the Cy7 molecule was oxidized and decomposed into two parts, inhibiting the LRET from UCNPs to Cy7; accordingly, the UCL of UCNPs at 800 nm was recovered (Figure 8c). The emission intensity at 800 nm was linearly correlated to the concentration of $ONOO^-$, demonstrating the potential for quantitative detection of $ONOO^-$. Thus, the UCNPs were used for in vivo detection of drug-induced hepatotoxicity in living mice. Different doses of APAP (500, 250 and 0 mg/kg) were intraperitoneally injected into living mice. The UCNPs were injected through the tail vein 15 minutes later. A remarkable enhancement of UCL signals in the liver region was detected for APAP-treated mice, while almost no UCL signals were observed from the control mice (Figure 8d). Meanwhile, the signal intensity was corresponded to the dosage of injected drug (Figure 8e). These observations demonstrated that the UCNPs were suitable for imaging drug-induced hepatotoxicity in living mice.

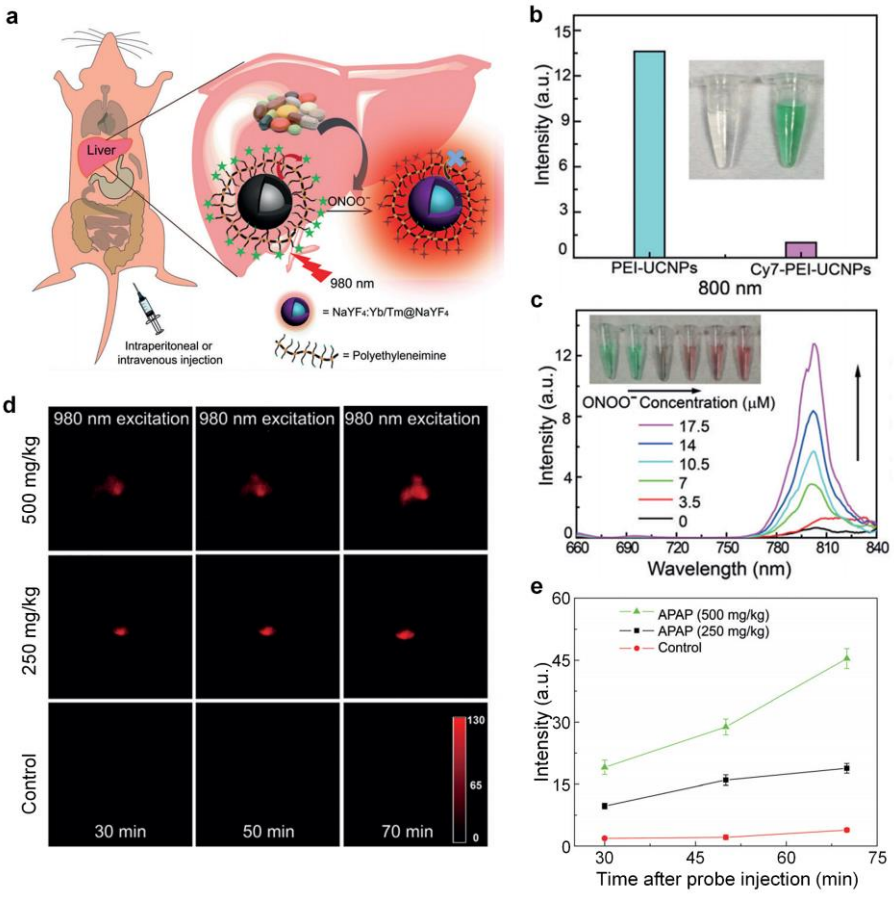

Figure 8. (a) Rational design of Cy7-assembled UCNPs for the detection of drug-induced hepatotoxicity in vivo. (b) UCL signals of nanoprobes at 800 nm before and after modification with Cy7. (c) The UCL spectrum of the nanoprobes with different concentration of $ONOO^-$. Inset: color change of the nanoprobes in the presence of $ONOO^-$. (d) Representative images of mice receiving nanoprobes pre-treated with 500, 250 mg kg^{-1} APAP or PBS at different time points. The images were collected at 790 nm upon irradiation at 980 nm. (e) The UCL intensity over time. The data were obtained from the liver area of images after subtracting the background. (n = 3 mice per group). Reprinted with permission from Ref. [71]. Copyright 2017, WILEY-VCH Verlag GmbH & Co. KGaA, Weinheim.

4 Chemiluminescence (CL) imaging

UCL imaging reduces tissue autofluorescence due to the excitation of NIR light. However, the short-wavelength emission of UCL limits the applications for deep-tissue imaging. Besides, the in vivo toxicity of UCNPs is a concern since the ions of the rare-earth metals in UCNPs are well known to be toxic. Chemiluminescence (CL) is the emission of luminescence that takes advantage of chemical reaction without real-time light excitation. Thus, CL imaging totally avoids the autofluorescence from the biological specimen, offering better penetration depth and higher signal-to-background ratio (SBR) than fluorescence imaging and UCL imaging [72-74]. Peroxalate chemiluminescence (POCL) reaction has been adopted for specific in vivo imaging of H_2O_2 [75-77]. Peroxalate compounds can be oxidized by H_2O_2 to form high energy 1,2-dioxetanedione intermediate that subsequently transfers its energy to nearby fluorophore to generate chemically ignited luminescence [78, 79].

Murthy et al. reported the peroxalate nanoparticles for imaging of H_2O_2, which were formulated from a hydrophobic polymer that contained peroxalate esters in its backbone and a fluorescent dye pentacene [75]. The resulting

peroxalate nanoparticles allowed for in vivo visualization of H_2O_2-associated inflammatory diseases. Similarly, Sehoon Kim et al. integrated all components needed for CL reaction into water-dispersed colloids for the specific imaging of H_2O_2 in vivo [74]. The nanoparticles were prepared through nanoprecipitation of bis[3,4,6-trichloro-2-(pentyloxycarbonyl)phenyl] oxalate (CPPO) as a chemiluminescent substrate, 3,3′-diethylthiadicarbocyanine iodide (Cy5) as a NIR dye, poly(lactic-co-glycolic acid) (PLGA) as a biocompatible polymer, and Pluronic F-127 as an amphiphilic functional polymer. The oxidation reaction occurred between CPPO and H_2O_2, resulting in the generation of 1,2-dioxetanedione intermediate to release energy to excite Cy5. This all-in-one POCL nanoparticles generated efficient CL for visualization of diseases associated with inflammation in living mice.

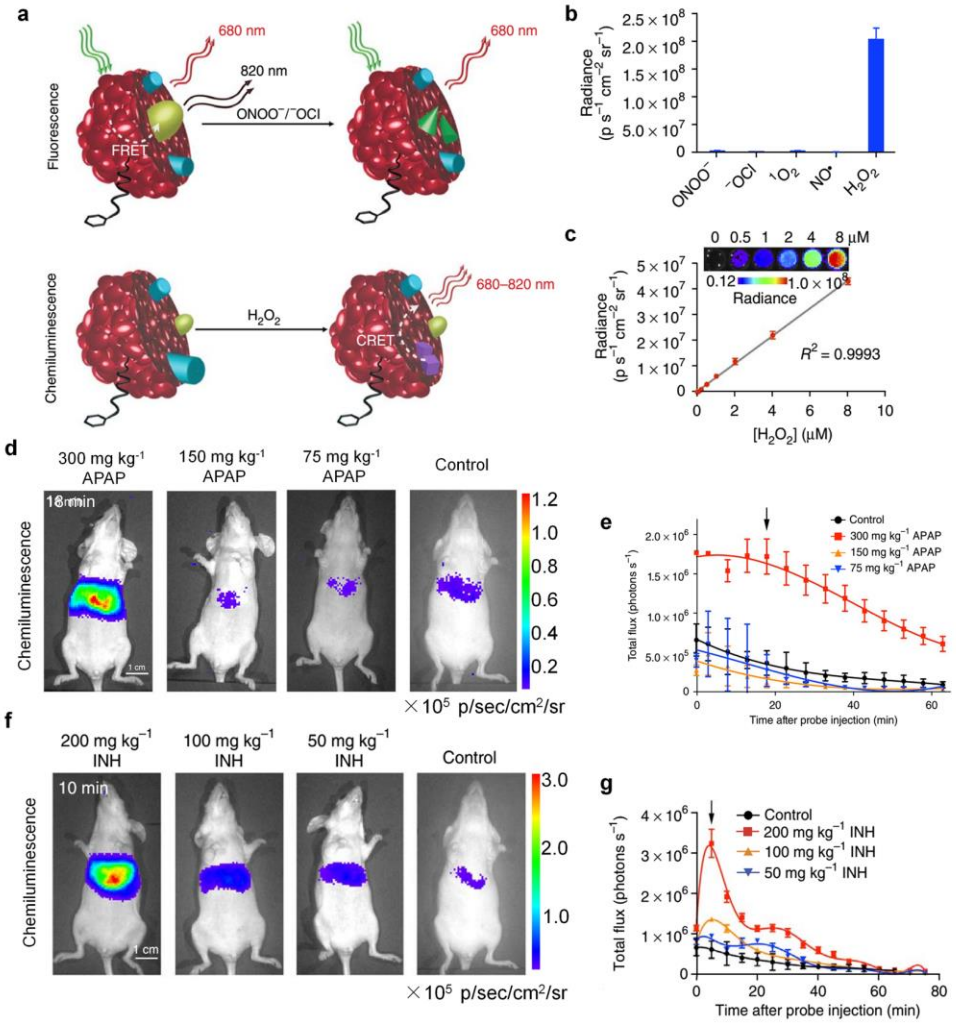

Figure 9. (a) Illustration of the mechanism of detection of $ONOO^-$ or ^-OCl and H_2O_2 by SPN-P3. (b) Specificity of CL signal of SPN-P3 determined in the presence of RONS. (c) CL response of SPN-P3 to different concentrations of H_2O_2. Inset, representative CL images of SPN-P3 response to different concentrations of H_2O_2. (d) Representative images of mice receiving APAP or saline (control) intraperitoneally, followed by SPN-P3 intravenously. (e) Emission intensities of the liver for CL over time. Black arrows indicate the respective time points shown in d. (f) Representative images of mice that received INH or saline (control) intraperitoneally followed by SPN-P3 intravenously. (g) Emission intensities of the liver for CL over time. Black arrows indicate the respective time points shown in (f). Reprinted with permission from Ref. [77]. Copyright 2014, Nature Publishing Group.

In addition to inflammatory diseases, H_2O_2-induced CL can be used for direct evaluation of drug-induced acute hepatotoxicity which is a common concern of modern medicine [77]. As we mentioned in the UCL imaging section, overdose of APAP could cause acute hepatotoxicity through oxidative and nitrosative stress to generate RONS. Isoniazid (INH), an anti-tuberculosis agent, is also associated with hepatotoxicity. The organic nanoprobe (SPN-P3) was synthesized through nanoprecipitation of poly (2,7-(9,9-dioctylfluorene)-alt-4,7-bis(thiophen-2-yl)benzo-2,1,3-thiadiazole) (P3), a RONS responsive NIR dye (IR775S), and a H_2O_2-reactive chemiluminescent substrate (CPPO). As we mentioned in the fluorescence imaging section, in the presence of $ONOO^-$ or ClO^-, IR775S could be irreversibly degraded and then FRET was abolished, leading to the emission enhancement at 680 nm (Figure 9a). In the presence of H_2O_2, the photons generated from the chemiluminescent reaction between CPPO and H_2O_2 induced luminescence without external excitation through chemiluminescence resonance energy transfer (CRET) (Figure 9a). The CRET was only triggered by H_2O_2, not by other RONS such as $ONOO^-$, ^-OCl, $^1O_2$, and $NO\cdot$ (Figure 9b). Moreover, the CL signals of SPN-P3 responded linearly to the concentration of H_2O_2 (Figure 9c). The capability of SPN-P3 for real-time imaging of APAP or INH induced hepatotoxicity was further tested in living mice (Figure 9d-g). The CL signals of SPN-P3 showed a significant enhancement for the mice challenged with overdose of APAP (300 mg kg^{-1}) (Figure 9d&e) or INH (threshold dose, 50 mg kg^{-1}) (Figure 9f&g). This proved that SPN-P3 could be used to monitor in vivo drug-induced hepatotoxicity.

Although POCL for in vivo imaging of H_2O_2 is a well-established approach, the mechanisms for optimizing CL have been rarely studied. Recently, Pu's group revealed the importance of energy level alignment between peroxalate and fluorophore in determining CL intensity [78]. Five polyfluorene-based polymer including P3, poly (9,9'-dioctyl-2,7-divinylenefluorenylene)-alt-(9,10-anthracene)) (P4), poly ((9,9'-dioctylfluorenyl-2,7-diyl)-alt-(benzo(2,1,3) thiadiazol-4,7-diyl)) (P5), poly ((9,9'-dioctyl-2,7-divinylenefluorenylene)-alt-(2-methoxy-5-(2-ethylhexyloxy)-1,4-phenylene)) (P6) and poly ((9,9'-dioctylfluorenyl-2,7-diyl) (P7) were chosen to prepare SPNs. Bis(2,4,6-trichlorophenyl) oxalate (TCPO), was chosen as a highly reactive peroxalate. The SPNs were prepared through nanoprecipitation of polymers, TCPO and an amphiphilic triblock copolymer (PEG-*b*-PPG-*b*-PEG). The CL signals of SPNs could be optimized according to the chemically initiated electron exchange luminescence (CIEEL) and the frontier molecular orbital theory (Figure 10a&b). In CIEEL, the oxidation reaction occurs between TCPO and H_2O_2, affording the high energy intermediate (HEI), 1,2-dioxetanedione. Through obtaining an electron from the SP, this HEI undergoes reduction reaction and forms SP radical cation and carbon dioxide radical anion. Then, back electron transfer occurs between the cation and anion to produce the excited SPs, resulting in the luminescence of SP. The intermolecular electron transfer from the SP to HEI is the key step of CIEEL to govern the CL efficacy of SPNs. The degree of freedom for the intermolecular electron transfer is determined by the energy interval between the highest occupied molecular orbital (HOMO) of SP and the lowest unoccupied molecular orbital (LUMO) of 1,2-dioxetanedione. According to Figure 10b, the HOMO of P6 was the closest to the LUMO of 1,2-dioxetanedione, resulting in the highest chemiluminescence quantum yield (QY) (2.30×10^{-2} E/mol). The CL QYs of SPNs were proportional to the energy interval between the HOMO of SP and LUMO of 1,2-dioxetanedione (Figure 10c). Thus, SPN-P6 efficiently detected H_2O_2 in vitro and the limit of detection was ~5 nM. The in vivo imaging of LPS-induced neuroinflammation in mouse model was successfully conducted using SPN-P6. In the consideration of safety, only 2 μL SPN-P6 solution

was administered via intracerebral injection to image H_2O_2 in neuroinflammation. The CL signal for LPS-treated mice was ~1.7-fold higher than that for the control, which was reduced by 21% upon GSH remediation (Figure 10d&e). This design not only provided a series of optical probes for ultrasensitive imaging of H_2O_2 in living mice but also revealed the underlying mechanism to optimize CL efficiency.

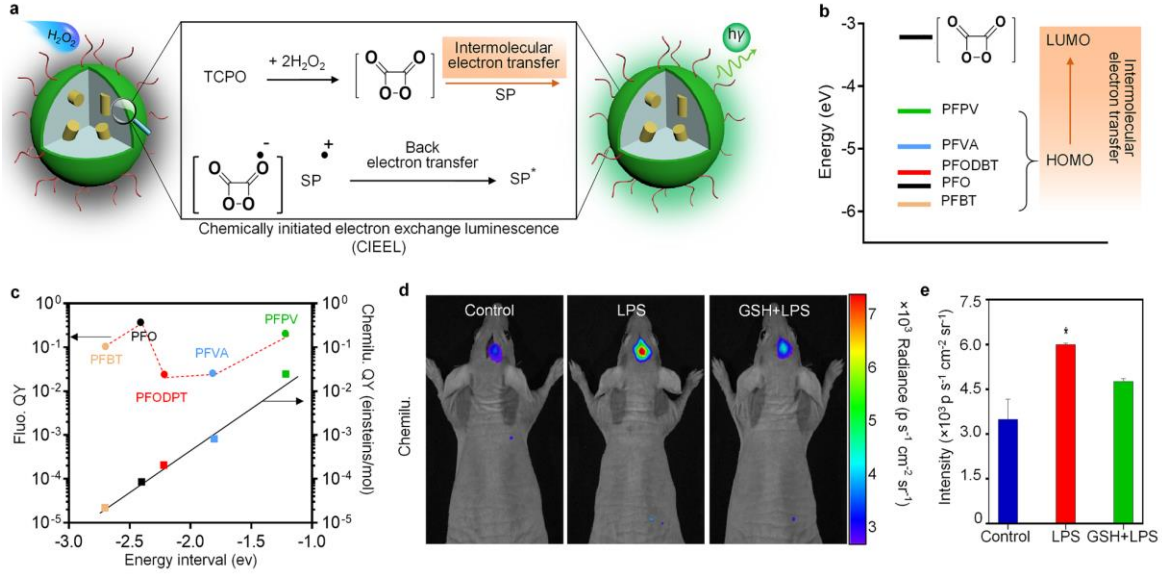

Figure 10. (a) Illustration of the chemically initiated electron exchange luminescence (CIEEL) mechanism of SPNs. (b) The LUMO level of 1,2-dioxentanedione and the HOMO levels of SPs. (c) The fluorescence and CL QYs of SPNs as a function of the energy intervals between the LUMO of 1,2-dioxentanedione and the HOMO of SPs. HOMO: −4.4 (PFPV), −5.0 (PFVA), −5.4 (PFODBT), −5.6 (PFO) and −5.9 ev (PFBT); the LUMO of 1,2-dioxetanedione is −3.2 ev. (d) Representative CL images of mice treated with saline, LPS or LPS with GSH, followed by intracerebral injection of SPN-P6 at 4 h later. (e) Quantification of CL signals calculated from the in vivo images in d. Reprinted with permission from Ref. [78]. Copyright 2016, American Chemical Society.

In addition to H_2O_2-induced POCL, CL can be triggered between the reaction of imidazopyrazinone (CLA) and superoxide radical ($O_2^{\cdot-}$) [80-82]. Tang et al. took advantage of this reaction to develop a nanoprobe to detect $O_2^{\cdot-}$ *via* CRET [83]. The nanoprobe (P8) was designed to comprise an $O_2^{\cdot-}$ reactive CL unit (CLA) as the energy donor and a SP (PFBT) with quaternary ammonium groups as the energy acceptor and signal amplification matrix. Upon reaction with $O_2^{\cdot-}$, the energy produced by the specific reaction between CLA and $O_2^{\cdot-}$ was transferred to PFBT, emitting the luminescence signal of SPN-P8 at 560 nm (Figure 11a). The CL intensities were linearly correlated to the concentrations of $O_2^{\cdot-}$ in the wide ranges of 0-950 pM (Figure 11b) with the limit of detection of 19.3 pM. Compared to the control SPN (P8 without PFBT), SPN-P8 showed a longer half-life of CL (Figure 11c). Therefore, SPN-P8 was used for CL imaging of $O_2^{\cdot-}$ in both LPS-induced inflammation model and tumor model in living mice. Much stronger CL signals in tumor tissues were detected after injection of SPN-P8, which was 3.0-time higher than that in normal tissue, demonstrating the high levels of $O_2^{\cdot-}$ in the tumor (Figure 11d&e). The CL signals in tumor were reduced after treatment with Tiron (a free-radical scavenger) due to the scavenging of $O_2^{\cdot-}$ (Figure 11d&e). Thus, SPN-P8 exhibited the potential to detect the variation of $O_2^{\cdot-}$ in living animals.

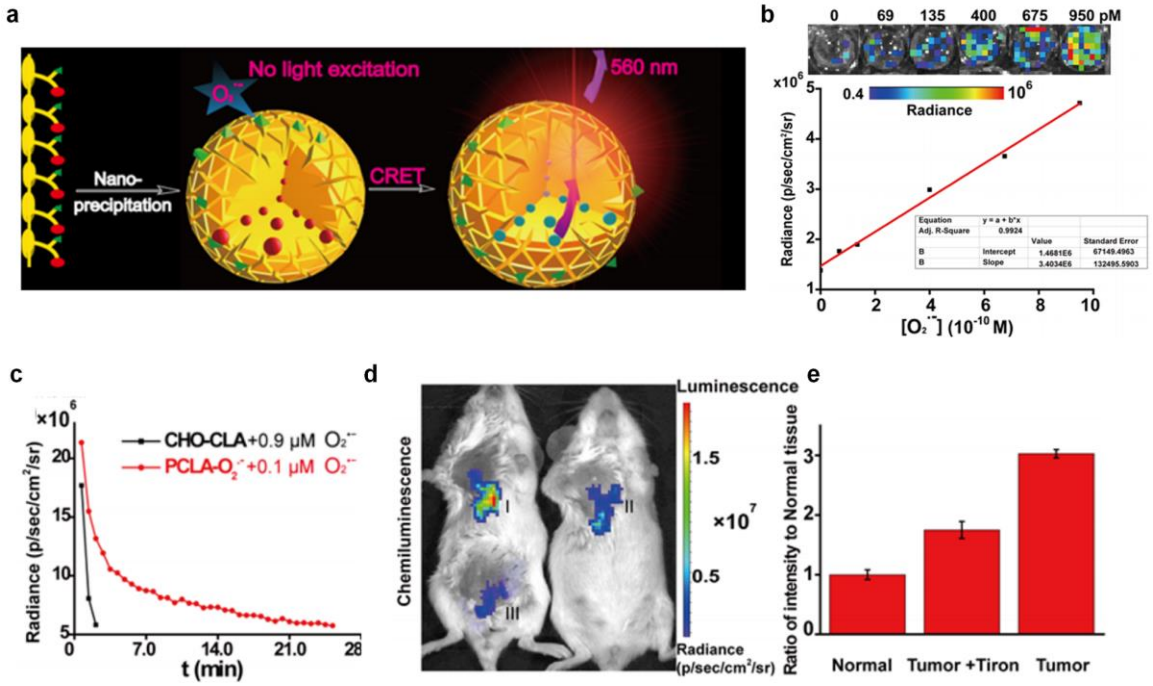

Figure 11. (a) Schematic illustration of SPN-P8 preparation by nanoprecipitation and the mechanism for detection of $O_2^{\cdot-}$. (b) Linear relationship between CL of SPN-P8 and [$O_2^{\cdot-}$] (0-950 pM). Inset: CL images of SPN-P8 in response to different concentrations of $O_2^{\cdot-}$. (c) Quantitative CL intensities of CHO-CLA and SPN-P8 as a function of time. (d) Representative CL images (pseudocolor) of mice in vivo tumor (I), tumor + Tiron (II) and normal (III) tissues followed by SPN-P8. Images were acquired using an IVIS Lumina II at 30 s after SPN-P8 administration. (e) Quantitative CL intensities of (I-III). Reprinted with permission from Ref. [83]. Copyright 2016, American Chemical Society.

5 Photoacoustic (PA) imaging

Due to the strong scattering of photons when passing through tissue, the tissue penetration depth of traditional optical imaging modalities is limited. Although nanoprobes with NIR absorption are used in traditional optical imaging, the tissue penetration depth is still limited within 1 cm [84, 85]. PA imaging is a hybrid non-ionizing imaging modality that capitalizes on the PA effect to integrate optical excitation with ultrasonic detection [86, 87]. During the PA imaging, endogenous chromophores or exogenous contrast agents are irradiated by short laser pulses, and then the photons are absorbed and partially converted to heat, producing broadband acoustic waves *via* thermos-elastic expansion [86]. These PA waves can be detected by ultrasound transducers outside the tissue and reconstructed into images of the absorbed optical energy distribution [88]. Because phonons are less scattered in tissue than photons, PA imaging has deeper in vivo imaging depth (up to 6 cm) and higher spatial resolution (as low as 5 μm) compared with traditional optical imaging modalities [89]. Many exogenous light absorbers including carbon nanotubes [90, 91], near-infrared dyes [92-94], gold nanoparticles [95], 2D materials [96], porphysomes [97], and semiconducting polymer nanoparticles [98-102] have been developed as contrast agents for PA imaging. However, most of the contrast agents only simply work as accumulation probes and their signals mainly result from accumulation via enhanced permeability and retention (EPR) effect or active targeting. In contrast, activatable PA probes response to intrinsic physiological signals have the advantages of low background noise and could provide critical information related to disease status [103, 104].

Therefore, application of PA imaging for detection of RONS has been conducted.

Pu and Rao et al. reported the first activatable ratiometric PA nanoprobe for in vivo imaging of RONS [105]. Poly(cyclopentadithiophene-alt-benzothiadiazole) (P9) and IR775S were used to prepare SPN-P9 *via* nanoprecipitation. IR775S could be rapidly oxidized by RONS such as $ONOO^-$ or ClO^-, as discussed in the fluorescence imaging section. The PA spectrum of SPN-P9 showed three peaks at 700 (P9), 735 (IR775S) and 820 (IR775S) nm. Upon addition of RONS such as $ONOO^-$ or ClO^-, the PA peaks at 735 and 820 nm decreased significantly, but the peak at 700 nm remained nearly the same, leading to the ratiometric PA imaging of RONS.

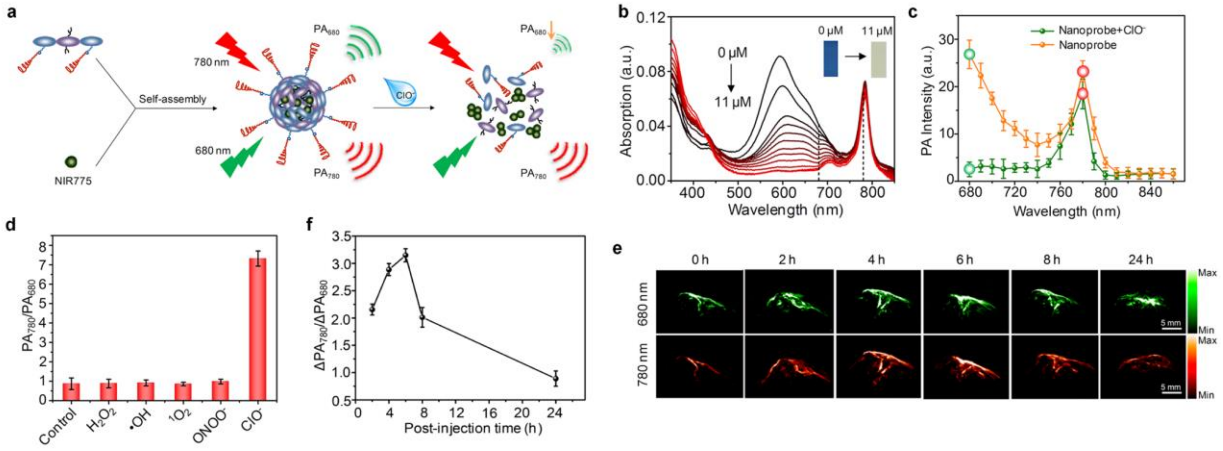

Figure 12. (a) Illustration of the synthesis of PA nanoprobe (SOA) and the sensing mechanism for SOA. (b) The absorption spectra of SOA upon addition of ClO- at intervals of 1 μM. (c) The PA spectra of SOA in the presence and absence of ClO^-. (d) Ratiometric PA responses (PA_{780}/PA_{680}) of SOA toward different ROS. (e) Representative PA images of subcutaneous 4T1 xenograft tumor before and 2, 4, 6, 8, and 24 h after intravenous administration of SOA in living mice. (f) Ratiometric PA signals ($\Delta PA_{780}/\Delta PA_{680}$) as a function of postinjection time of SOA. Reprinted with permission from Ref. [106]. Copyright 2017, American Chemical Society.

To enhance the specificity of activatable nanoprobes towards ClO^-, Pu's group further designed an activatable PA nanoprobe based on SO3 for ratiometric PA imaging of ClO^- [106]. SO3 had the phenothiazine structure in the semiconducting backbone which could be oxidized by ClO^-. PEG was used as the side chains to provide water solubility and spontaneously encapsulate a RONS-inert NIR dye (NIR775) through self-assembly to form semiconducting organic amphiphile (SOA) (Figure 12a). The SOA had two absorption peaks with the maxima at 596 and 784 nm which were assigned to the absorption of SO3 and NIR775, respectively (Figure 12b). With increasing concentration of ClO^-, the absorption peak at 596 nm decreased gradually, while the absorption peak at 784 nm remained almost unchanged (Figure 12b). The PA spectrum of SOA also showed the same response towards ClO^- (Figure 12c). The ratiometric PA signal (PA_{780}/PA_{680}) increased linearly with the concentration of ClO^-. Meanwhile, such a ratiometric PA signal only responded toward ClO^-, not other RONS including H_2O_2, ·OH, $^1O_2$, and $ONOO^-$ (Figure 12d). The capability of SOA for in vivo imaging of ClO^- was further tested using subcutaneous 4T1 xenograft tumor model. The PA images at the tumor region were recorded at 680 and 780 nm, which were indicated in pseudo green and red colors, respectively (Figure 12e). The PA signal at 780 nm of the tumor increased significantly over time after intravenous injection of SOA and reached the maximum at 6 h postinjection. However, the PA signal at 680 nm increased slightly. As NIR775 was

insensitive to ClO^-, the strong PA intensity increment at 780 nm was attributed to the EPR effect of SOA. The slight PA intensity increment at 680 nm indicated the degradation of SOA by ClO^- in the tumor microenvironment. Therefore, the ratiometric PA signals ($\Delta PA_{780}/\Delta PA_{680}$) gradually increased over time and reached the maximum at 6 h postinjection (Figure 12f). This design clearly indicated the capability of SOA to detect ClO^- in the tumor region of living mice.

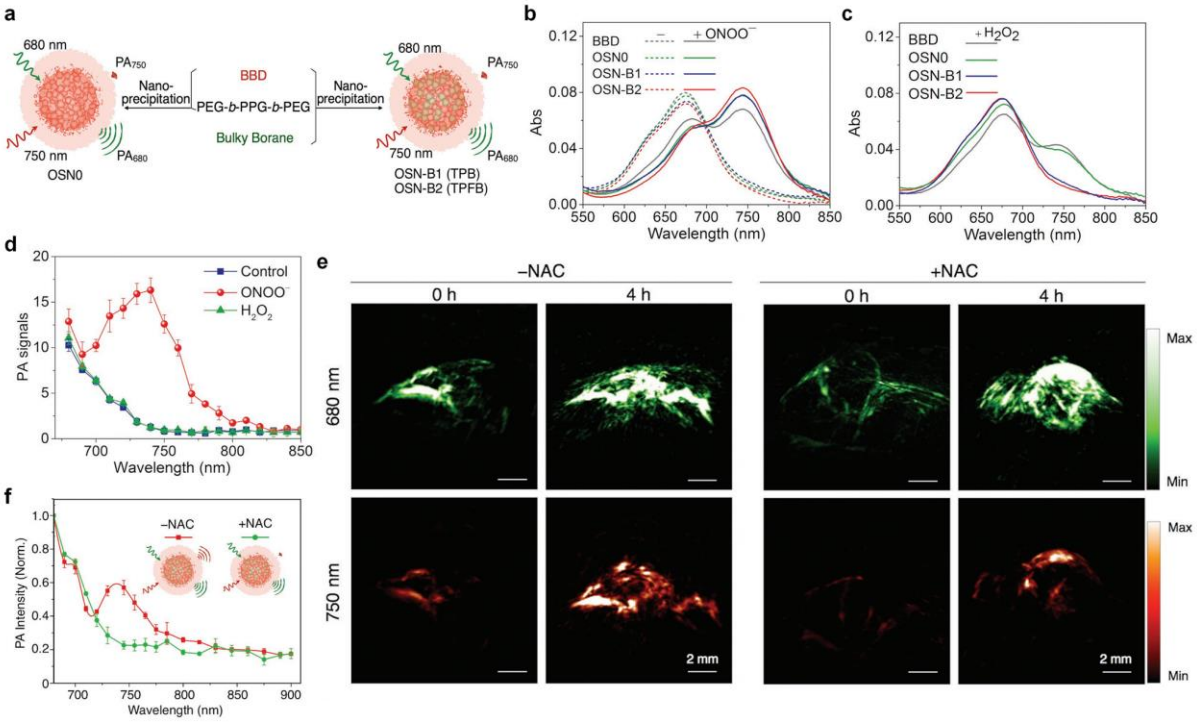

Figure 13. (a) Schematic illustration for the preparation of OSNs via nanoprecipitation. The absorption of OSNs and BBD upon addition of $ONOO^-$ (b) or H_2O_2 (c). (d) The PA spectra of OSN-B1 before and after addition of $ONOO^-$ or H_2O_2. (e) Representative PA images of subcutaneous 4T1 xenograft tumor of NAC-treated and untreated mice after intravenous administration of OSN-B1. (f) The real-time PA spectra of tumor in NAC-treated and untreated mice after intravenous administration of OSB-B1 at 4 h. Reprinted with permission from Ref. [107]. Copyright 2017, WILEY-VCH Verlag GmbH & Co. KGaA, Weinheim.

To realize the specific and selective PA imaging of $ONOO^-$, organic semiconducting nanoprobes doped with bulky borane has been developed [107]. Boronate-caged boron-dipyrromethene (BBD) can be activated by both $ONOO^-$ and H_2O_2, and its deboronated phenoxide product is pH sensitive, which limits the application of BBD for in vivo imaging of $ONOO^-$. To overcome these limitations, another sensing component triphenylborane (TPB) or tris(pentafluorophenyl)borane (TPFB) was doped with BBD to form a $ONOO^-$ specific activatable PA nanoprobe (Figure 13a). The absorption spectra of all the nanoprobes were nearly the same with a maximum peak at 675 nm (Figure 13b). The bulky borane (TPB or TPFB) within the nanoprobe served as the $ONOO^-$degradable but H_2O_2-inert shield for BBD, which inhibited the reaction between BBD and H_2O_2 due to its stronger oxidative capability. Therefore, the absorption of all the nanoprobes at 675 nm gradually decreased with the concomitant appearance of a new peak at 745 nm upon addition of $ONOO^-$ (Figure 13b). In contrast, only BBD and OSN0 increased the ratiometric absorption signals (Ab_{745}/Ab_{675}) in the presence of H_2O_2, while OSN-B1 and OSN-B2 remained nearly the same (Figure 13c). Due to the higher $ONOO^-$ selectivity and faster kinetics relative

to other probes, OSN-B1 was chosen for PA imaging. Upon addition of $ONOO^-$, the PA signal of OSN-B1 at 750 nm significantly increased while the signal at 680 nm remained almost unchanged (Figure 13d). The in vivo PA imaging of $ONOO^-$ using OSN-B1 was tested on subcutaneous 4T1 xenograft tumor of living mice. NAC was used to reduce ROS level at tumor site. The PA increment at 680 nm (ΔPA_{680}) in the tumors for both NAC-treated and untreated mice should be assigned to the accumulation of OSN-B1, while the PA increment at 750 nm (ΔPA_{750}) revealed the partial activation of OSN-B1 by $ONOO^-$ in the tumor region occurred during the accumulation of OSN-B1. Therefore, the in vivo ratiometric signal ($\Delta PA_{750}/\Delta PA_{680}$) reached its maximum at 4 h postinjection for the untreated mice, while only a slight increase for NAC-treated mice, implying the efficient activation of OSN-B1 in the untreated mice (Figure 13e). The PA spectra of tumors at 4 h for both NAC-treated and untreated mice also indicated the ability of OSN-B1 to in vivo track the variation of $ONOO^-$ in real time.

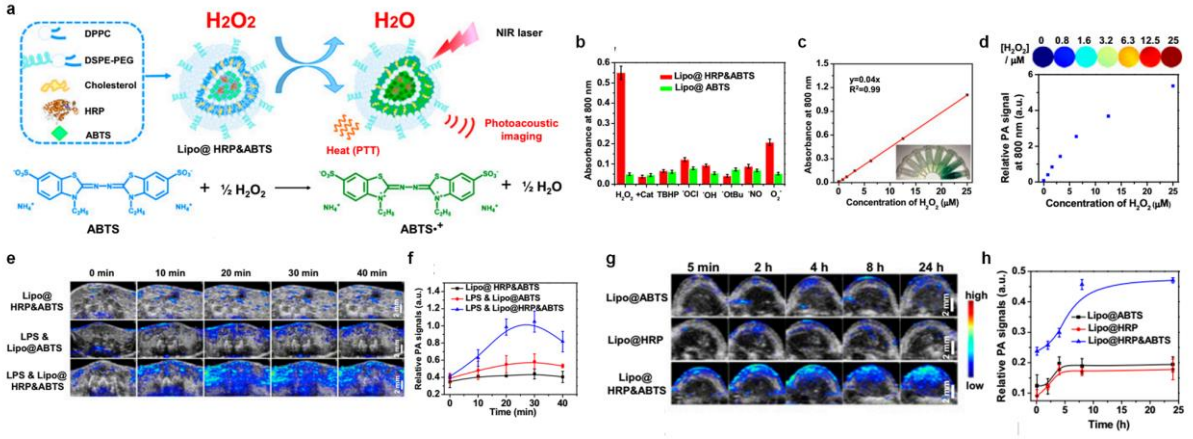

Figure 14. (a) Schematic illustration of the preparation of Lipo@HRP&ABTS and the mechanisms for PA imaging of H_2O_2. (b) The absorbance of Lipo@HRP&ABTS or Lipo@ABTS at 800 nm after incubation with different types of ROS. (c) The absorbance of Lipo@HRP&ABTS at 800 nm after incubation with different concentrations of H_2O_2. (d) The PA images (Top) and PA signal intensities at 800 nm (Bottom) of Lipo@HRP&ABTS with different concentrations of H_2O_2. (e) The representative PA images of mouse abdomen at 24 h after injection of LPS to induce inflammation with i.p. injection of Lipo@HRP&ABTS or Lipo@ABTS. (f) PA signals for mouse abdomen based on PA imaging data in (e). (g) The representative PA images of subcutaneous 4T1 xenograft tumor 5 min, 2, 4, 8, and 24 h after i.v. injection of Lipo@ABTS, Lipo@HRP, and Lipo@HRP&ABTS. (h) PA signals in tumors based on PA imaging data in (g). Reprinted with permission from Ref. [108]. Copyright 2017, National Academy of Sciences.

In addition to ratiometric PA imaging of RONS, activatable PA probe from "off" to "on" state in a single channel has been developed [108]. Horseradish peroxidase (HRP) and its substrate, 2,2′-azino-bis(3-ethylbenzothiazoline-6-sulfonic acid) (ABTS), were co-encapsulated into a liposomal nanoprobe (Lipo@HRP&ABTS). Upon addition of H_2O_2, the encapsulated HRP in the nanoprobe could catalyze colorless ABTS into its green oxidized form, and thus the nanoprobe could display strong PA signals (Figure 14a). All types of ROS could not induce appreciable absorbance change for the nanoprobe (Lipo@ABTS) without HRP (Figure 14b). In contrast, upon addition of H_2O_2, the Lipo@HRP&ABTS showed significantly increased NIR absorbance, while no obvious change was detected for H_2O_2 on the presence of catalase or other types of ROS including tert-butyl hydroperoxide (TBHP), ClO^-, $\cdot OH$, $\cdot OtBu$ and $NO\cdot$ except for $O_2^{\cdot-}$, which only induced a slight change (Figure 14b). The absorption intensity of Lipo@HRP&ABTS at 800 nm increased linearly upon addition of different concentrations of H_2O_2 (Figure

14c). The PA signals of Lipo@HRP&ABTS at 800 nm also showed an enhanced tendency with increasing H_2O_2 concentration (Figure 14d). The limit of detection for H_2O_2 was determined to be 0.8 μM. Therefore, such nanoprobe was demonstrated for in vivo detection of LPS-induced inflammation (Figure 14e&f), bacterial infection, 4T1 subcutaneous tumor (Figure 14g&h), orthotopic brain glioma tumor, and lymphatic metastasis tumor with high specificity and sensitivity.

The molecular self-assembly which transforms small molecules or nanoparticles into high-order complexes provides a strategy for in vivo imaging of RONS [109]. Phthalocyanine and PEG were covalently linked by the phenylboronic acid pinacol ester groups to form an amphiphilic semiconducting macromolecule, zinc-tetra(2-((1-(3-amino-3-oxopropyl)-1H-1,2,3-triazol-4-yl)-methoxy)-2-oxo-1-(4-((4-(4,4,5,5-tetramethyl-1,3,2-dioxaborolan-2-yl)benzyl)oxy)phenyl)ethyl methoxy poly(ethylene glycol) succinate)phthalocyanine (PCBP). The control nanoprobe without the ROS linker, zinc-tetra(3-(4-((methoxy poly(ethylene glycol))methyl)-1H-1,2,3-triazol-1-yl)-propenamide)phthalocyanine (PCP) was also synthesized. The aryl boronic ester group could be oxidized by RONS including H_2O_2 and $ONOO^-$ [110], cleaving hydrophilic PEG from PCBP. The residual phthalocyanine segments self-assembled and regrew into large nanoparticles owing to the enhanced hydrophobic interaction and π-π stacking. The large nanoparticles had increased PA signals as compared with small nanoparticles, due to enhanced heat transfer for large nanoparticles (Figure 15a) [111-113]. The obtained two nanoprobes (PCP and PCBP) had similar hydrodynamic sizes (18 ± 6 and 20 ± 2 nm, respectively) and similar PA spectra under the same mass concentration of phthalocyanine. In the presence of H_2O_2, the size of PCBP increased gradually, while the size of the control probe PCP remained nearly the same. This indicated that the increased size of PCBP was attributed to the ROS-induced cleavage of PEG chain to enhance hydrophobicity and PCBPs to regrow into large nanoparticles (Figure 15b). There was no significant size change when PCBP was treated with other ROS including ·OH, $^1O_2$, -OCl, and O_2^- except for $ONOO^-$, which could also react with boronate moiety to increase the size of PCBP. Therefore, PCBP was used for in vivo PA imaging of RONS in the subcutaneous 4T1 xenograft tumor of living mice. D,L-Buthionine-(*S*,*R*)-sulphoximine (BSO), an inhibitor that depletes glutathione, was used to elevate the ROS level at tumor site. The PA increment at 700 nm (ΔPA_{700}) in the tumors for both BSO-treated and untreated mice substantially increased and reached the maximum at 8 h post-injection of PCBP for both mice (Figure 15c). Meanwhile, at each time point, ΔPA_{700} for BSO-treated mice was higher than that of untreated mice. At t = 8 h, ΔPA_{700} for BSO-treated mice was 2.0-fold higher than that of untreated mice, implying that the self-assembly of PCBP was activated by the elevated ROS in the tumor of BSO-treated mice. This study provided a RONS-triggered self-assembly approach to develop activatable nanoprobe for enhanced PA imaging.

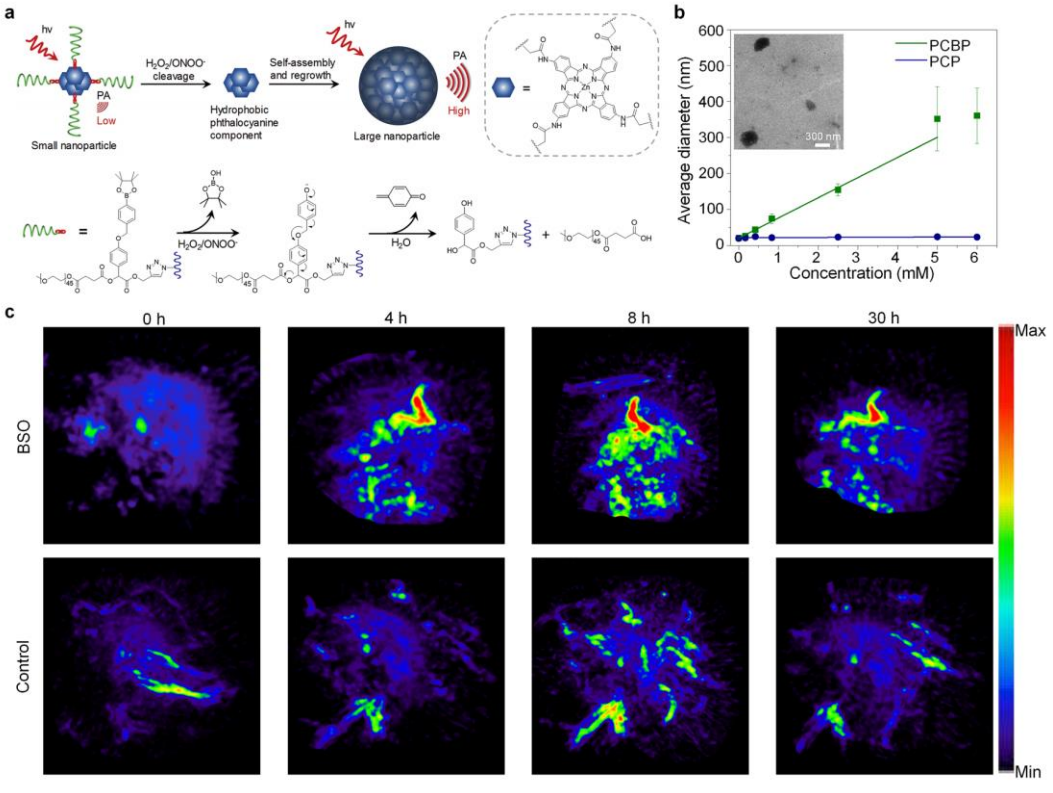

Figure 15. (a) Design and mechanism of the self-assembly probe (PCBP) for PA imaging of ROS. (b) Average diameters of PCBP and PCP with different concentrations of H_2O_2. Inset: TEM image of PCBP after addition of H_2O_2 (5 mM). (c) Representative PA images of subcutaneous 4T1 xenograft tumor of BSO-treated and untreated mice before and after intravenous administration of PCBP. Reprinted with permission from Ref. [109]. Copyright 2017, WILEY-VCH Verlag GmbH & Co. KGaA, Weinheim.

6 Summary and Outlook

This review summarizes the recent progress on optical nanoprobes for molecular imaging of RONS in living organisms. The imaging modalities include fluorescence, UCL, CL and PA imaging. RONS-responsive activatable nanoprobes are usually developed through conjugation or incorporation of RONS-sensitive components. In the presence of RONS, the RONS-responsive part of the nanoprobes is cleaved or decomposed, leading to the alteration or recovery of fluorescence, UCL or PA signals (Figure 16).

Although activatable nanoprobes for in vivo detection of RONS have achieved significant progress, there are still several important issues that should be addressed in terms of materials design. For instance, although the organic nanoprobes are completely organic and have been reported to show minimal cytotoxicity and even good in vivo biocompatibility, their long-term physiological effects require careful investigation. Similarly, the cytotoxicity and in vivo toxicity of the inorganic nanoparticles such as UCNPs should be concerned although the doping concentrations of rare-earth metals in UCNPs are relatively low. New materials design to further improve in the signal intensities of nanoprobes could help minimize potential toxicity because the dosages of nanoprobes can be minimized.

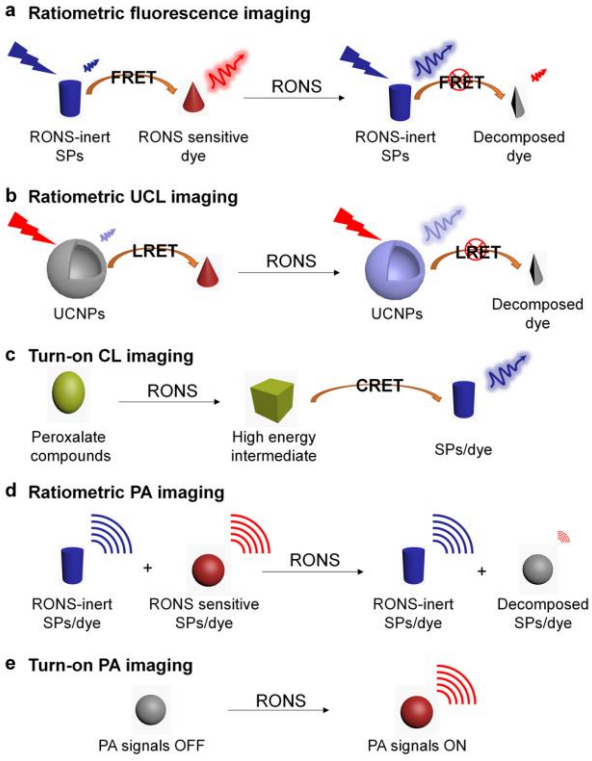

Figure 16. Schematic illustration of the design principles of RONS-responsive activatable nanoprobes. (a) Ratiometric fluorescence imaging. (b) Ratiometric UCL imaging. (c) Turn-on CL imaging. (d) Ratiometric PA imaging. (e) Turn-on PA imaging.

Although the current research focus is to develop specific optical nanoprobes, their imaging applications can be exploited for other diseases. For instance, the aberrant generation of RONS is reported for neurodegenerative diseases such as Alzheimer's, Parkinson's and Huntington's diseases. However, activatable nanoprobes for the early detection of neurodegenerative diseases are rarely reported, because of the difficulty in the penetration and accumulation of probes in brain. Surface modification of activatable nanoprobes with targeting molecules could help them across the blood-brain barrier (BBB) and enhance their brain uptake. On the other hand, the imaging applications can be broadened if the imaging depth and sensitivity can be enhanced through emerging photonic imaging technologies such as second-near-infrared window optical imaging [114].

Acknowledgements

K.P. thanks Nanyang Technological University (Start-Up grant: NTUSUG: M4081627.120) and Singapore Ministry of Education (Academic Research Fund Tier 1: RG133/15 M4011559 and 2015-T1-002-091; and Tier 2 MOE2016-T2-1-098) for the financial support.

References

[1] Dickinson, B. C.; Chang, C. J. Chemistry and biology of reactive oxygen species in signaling or stress responses. *Nat. Chem. Biol.* **2011**, *7*, 504-511.

[2] D'Autréaux, B.; Toledano, M. B. ROS as signalling molecules: mechanisms that generate specificity in ROS homeostasis. *Nat. Rev. Mol. Cell Biol.* **2007**, *8*, 813-824.

[3] Nathan, C.; Cunningham-Bussel, A. Beyond oxidative stress: an immunologist's guide to reactive oxygen species. *Nat. Rev. Immunol.* **2013**, *13*, 349-361.

[4] Weseler, A. R.; Bast, A. Oxidative stress and vascular function: implications for pharmacologic treatments. *Curr. Hypertens. Rep.* **2010**, *12*, 154-161.

[5] Newsholme, P.; Cruzat, V. F.; Keane, K. N.; Carlessi, R.; de Bittencourt, P. I. H. Molecular mechanisms of ROS production and oxidative stress in diabetes. *Biochem. J.* **2016**, *473*, 4527-4550.

[6] Thornton, C.; Baburamani, A. A.; Kichev, A.; Hagberg, H. Oxidative stress and endoplasmic reticulum (ER) stress in the development of neonatal hypoxic–ischaemic brain injury. *Biochem. Soc. T.* **2017**, BST20170017.

[7] Wen, T.; Zhang, H.; Chong, Y.; Wamer, W. G.; Yin, J.-J.; Wu, X. Probing hydroxyl radical generation from H 2 O 2 upon plasmon excitation of gold nanorods using electron spin resonance: Molecular oxygen-mediated activation. *Nano Res.* **2016**, *9*, 1663-1673.

[8] Pravalika, K.; Sarmah, D.; Kaur, H.; Wanve, M.; Saraf, J.; Kalia, K.; Borah, A.; Yavagal, D. R.; Dave, K. R.; Bhattacharya, P. Myeloperoxidase and Neurological disorder: A crosstalk. *ACS Chem. Neurosci.* **2018**, *9*, 421-430.

[9] Lundberg, J. O.; Gladwin, M. T.; Weitzberg, E. Strategies to increase nitric oxide signalling in cardiovascular disease. *Nat. Rev. Drug Discov.* **2015**, *14*, 623-641.

[10] Schieber, M.; Chandel, N. S. ROS function in redox signaling and oxidative stress. *Curr. Biol.* **2014**, *24*, R453-R462.

[11] Weidinger, A.; Kozlov, A. V. Biological activities of reactive oxygen and nitrogen species: oxidative stress versus signal transduction. *Biomolecules* **2015**, *5*, 472-484.

[12] Gonçalves, N. P.; Vægter, C. B.; Andersen, H.; Østergaard, L.; Calcutt, N. A.; Jensen, T. S. Schwann cell interactions with axons and microvessels in diabetic neuropathy. *Nat. Rev. Neurol.* **2017**, *13*, 135-147.

[13] Rani, V.; Deep, G.; Singh, R. K.; Palle, K.; Yadav, U. C. Oxidative stress and metabolic disorders: Pathogenesis and therapeutic strategies. *Life Sci.* **2016**, *148*, 183-193.

[14] Gaki, G. S.; Papavassiliou, A. G. Oxidative stress-induced signaling pathways implicated in the pathogenesis of Parkinson's disease. *Neuromol. Med.* **2014**, *16*, 217-230.

[15] Sabharwal, S. S.; Schumacker, P. T. Mitochondrial ROS in cancer: initiators, amplifiers or an Achilles' heel? *Nat. Rev. Cancer* **2014**, *14*, 709-721.

[16] Van Gaal, L. F.; Mertens, I. L.; Christophe, E. Mechanisms linking obesity with cardiovascular disease. *Nature* **2006**, *444*, 875-880.

[17] Wojtala, A.; Bonora, M.; Malinska, D.; Pinton, P.; Duszynski, J.; Wieckowski, M. R. Methods to monitor ROS production by fluorescence microscopy and fluorometry. In *Method. Enzymol.* . Elsevier, 2014; pp 243-262.

[18] Giraldo, J. P.; Landry, M. P.; Faltermeier, S. M.; McNicholas, T. P.; Iverson, N. M.; Boghossian, A. A.; Reuel, N. F.; Hilmer, A. J.; Sen, F.; Brew, J. A. Plant nanobionics approach to augment photosynthesis and biochemical sensing. *Nat. Mater.* **2014**, *13*, 400-408.

[19] Chen, G. Y.; Nuñez, G. Sterile inflammation: sensing and reacting to damage. *Nat. Rev. Immunol.* **2010**, *10*, 826-837.

[20] Heller, D. A.; Jin, H.; Martinez, B. M.; Patel, D.; Miller, B. M.; Yeung, T.-K.; Jena, P. V.; Höbartner, C.; Ha, T.; Silverman, S. K.; Strano, M. S. Multimodal optical sensing and analyte specificity using single-walled carbon nanotubes. *Nat. Nanotechnol.* **2009**, *4*, 114-120.

[21] Miller, E. W.; Tulyathan, O.; Isacoff, E. Y.; Chang, C. J. Molecular imaging of hydrogen peroxide produced for cell signaling. *Nat. Chem. Biol.* **2007**, *3*, 263-267.

[22] Chan, J.; Dodani, S. C.; Chang, C. J. Reaction-based small-molecule fluorescent probes for chemoselective bioimaging. *Nat. Chem.* **2012**, *4*, 973-984.

[23] Dickinson, B. C.; Srikun, D.; Chang, C. J. Mitochondrial-targeted fluorescent probes for reactive oxygen species. *Curr. Opin. Chem. Biol.* **2010**, *14*, 50-56.

[24] Hyman, L. M.; Franz, K. J. Probing oxidative stress: Small molecule fluorescent sensors of metal ions, reactive oxygen species, and thiols. *Coordin. Chem. Rev.* **2012**, *256*, 2333-2356.

[25] Yuan, L.; Lin, W.; Zheng, K.; Zhu, S. FRET-based small-molecule fluorescent probes: rational design and bioimaging applications. *Accounts Chem. Res.* **2013**, *46*, 1462-1473.

[26] Urano, Y. Novel live imaging techniques of cellular functions and in vivo tumors based on precise design of small molecule-based 'activatable'fluorescence probes. *Curr. Opin. Chem. Biol.* **2012**, *16*, 602-608.

[27] Chen, X.; Wang, F.; Hyun, J. Y.; Wei, T.; Qiang, J.; Ren, X.; Shin, I.; Yoon, J. Recent progress in the development of fluorescent, luminescent and colorimetric probes for detection of reactive oxygen and nitrogen species. *Chem. Soc. Rev.* **2016**, *45*, 2976-3016.

[28] Kowada, T.; Maeda, H.; Kikuchi, K. BODIPY-based probes for the fluorescence imaging of biomolecules in living cells. *Chem. Soc. Rev.* **2015**, *44*, 4953-4972.

[29] Kim, H. M.; Cho, B. R. Small-molecule two-photon probes for bioimaging applications. *Chem. Rev.* **2015**, *115*, 5014-5055.

[30] Smith, A. M.; Duan, H.; Mohs, A. M.; Nie, S. Bioconjugated quantum dots for in vivo molecular and cellular imaging. *Adv. Drug Deliver. Rev.* **2008**, *60*, 1226-1240.

[31] Zhou, J.; Liu, Z.; Li, F. Upconversion nanophosphors for small-animal imaging. *Chem. Soc. Rev.* **2012**, *41*, 1323-1349.

[32] Koo, H.; Huh, M. S.; Ryu, J. H.; Lee, D.-E.; Sun, I.-C.; Choi, K.;Kim, K.; Kwon, I. C. Nanoprobes for biomedical imaging in living systems. *Nano Today* **2011**, *6*, 204-220.

[33] Sun, T.; Zhang, Y. S.; Pang, B.; Hyun, D. C.; Yang, M.; Xia, Y. Engineered nanoparticles for drug delivery in cancer therapy. *Angew. Chem. Int. Edit.* **2014**, *53*, 12320-12364.

[34] Blanco, E.; Shen, H.; Ferrari, M. Principles of nanoparticle design for overcoming biological barriers to drug delivery. *Nat. Biotechnol.* **2015**, *33*, 941.

[35] Zhen, X.; Tao, Y.; An, Z.; Chen, P.; Xu, C.; Chen, R.; Huang, W.; Pu, K. Ultralong phosphorescence of water-soluble organic nanoparticles for in vivo afterglow imaging. *Adv. Mater.* **2017**, *29*, 1606665.

[36] Zhen, X.; Xie, C.; Pu, K. Temperature-correlated afterglow of a semiconducting polymer nanococktail for imaging-guided photothermal therapy. *Angew. Chem. Int. Edit.* **2018**, *57*, 3938-3942.

[37] Li, J.; Rao, J.; Pu, K. Recent progress on semiconducting polymer nanoparticles for molecular imaging and cancer phototherapy. *Biomaterials* **2018**, *155*, 217-235.

[38] Michalet, X.; Pinaud, F.; Bentolila, L.; Tsay, J.; Doose, S.; Li, J.; Sundaresan, G.; Wu, A.; Gambhir, S.; Weiss, S. Quantum dots for live cells, in vivo imaging, and diagnostics. *Science* **2005**, *307*, 538-544.

[39] Chen, M.; Yin, M. Design and development of fluorescent nanostructures for bioimaging. *Prog. Polym. Sci.* **2014**, *39*, 365-395.

[40] Wu, C.; Hansen, S. J.; Hou, Q.; Yu, J.; Zeigler, M.; Jin, Y.; Burnham, D. R.; McNeill, J. D.; Olson, J. M.; Chiu, D. T. Design of highly emissive polymer dot bioconjugates for in vivo tumor targeting. *Angew. Chem. Int. Edit.* **2011**, *50*, 3430-3434.

[41] Hu, S.-H.; Gao, X. Nanocomposites with spatially separated functionalities for combined imaging and magnetolytic therapy. *J. Am. Chem. Soc.* **2010**, *132*, 7234-7237.

[42] Zhou, W.; Gao, X.; Liu, D.; Chen, X. Gold nanoparticles for in vitro diagnostics. *Chem. Rev.* **2015**, *115*, 10575-10636.

[43] Chan, M.-H.; Lin, H.-M. Preparation and identification of multifunctional mesoporous silica nanoparticles for in vitro and in vivo dual-mode imaging, theranostics, and targeted tracking. *Biomaterials* **2015**, *46*, 149-158.

[44] Feng, T.; Ai, X.; An, G.; Yang, P.; Zhao, Y. Charge-convertible carbon dots for imaging-guided drug delivery with enhanced in vivo cancer therapeutic efficiency. *ACS Nano* **2016**, *10*, 4410-4420.

[45] Fan, Z.; Sun, L.; Huang, Y.; Wang, Y.; Zhang, M. Bioinspired fluorescent dipeptide nanoparticles for targeted cancer cell imaging and real-time monitoring of drug release. *Nat. Nanotechnol.* **2016**, *11*, 388-394.

[46] Chinen, A. B.; Guan, C. M.; Ferrer, J. R.; Barnaby, S. N.; Merkel, T. J.; Mirkin, C. A. Nanoparticle probes for the detection of cancer biomarkers, cells, and tissues by fluorescence. *Chem. Rev.* **2015**, *115*, 10530-10574.

[47] Wolfbeis, O. S. An overview of nanoparticles commonly used in fluorescent bioimaging. *Chem. Soc. Rev.* **2015**, *44*, 4743-4768.

[48] Lyu, Y.; Pu, K. Recent advances of activatable molecular probes based on semiconducting polymer nanoparticles in sensing and imaging. *Adv. Sci.* **2017**.

[49] Pu, K.; Shuhendler, A. J.; Rao, J. Semiconducting polymer nanoprobe for in vivo imaging of reactive oxygen and nitrogen species. *Angew. Chem. Int. Edit.* **2013**, *52*, 10325-10329.

[50] Wu, L.; Wu, I.-C.; DuFort, C. C.; Carlson, M. A.; Wu, X.; Chen, L.; Kuo, C.-T.; Qin, Y.; Yu, J.; Hingorani, S. R.; Chiu, D. T. Photostable ratiometric pdot probe for in vitro and in vivo imaging of hypochlorous acid. *J. Am. Chem. Soc.* **2017**, *139*, 6911-6918.

[51] Yin, C.; Zhu, H.; Xie, C.; Zhang, L.; Chen, P.; Fan, Q.; Huang, W.; Pu, K. Organic nanoprobe cocktails for multilocal and multicolor fluorescence imaging of reactive oxygen species. *Adv. Funct. Mater.* **2017**, *27*, 1700493.

[52] Ju, J.; Chen, W. In situ growth of surfactant-free gold nanoparticles on nitrogen-doped graphene quantum dots for electrochemical detection of hydrogen peroxide in biological environments. *Anal. Chem.* **2015**, *87*, 1903-1910.

[53] Gao, X.; Ding, C.; Zhu, A.; Tian, Y. Carbon-dot-based ratiometric fluorescent probe for imaging and biosensing of superoxide anion in live cells. *Anal. Chem.* **2014**, *86*, 7071-7078.

[54] Xu, H.; Suslick, K. S. Water-Soluble fluorescent silver nanoclusters. *Adv. Mater.* **2010**, *22*, 1078-1082.

[55] Chen, L.-Y.; Wang, C.-W.; Yuan, Z.; Chang, H.-T. Fluorescent gold nanoclusters: recent advances in sensing and imaging. *Anal. Chem.* **2014**, *87*, 216-229.

[56] Chen, T.; Hu, Y.; Cen, Y.; Chu, X.; Lu, Y. A dual-emission fluorescent nanocomplex of gold-cluster-decorated silica particles for live cell imaging of highly reactive oxygen species. *J. Am. Chem. Soc.* **2013**, *135*, 11595-11602.

[57] Liu, Q.; Feng, W.; Yang, T.; Yi, T.; Li, F. Upconversion luminescence imaging of cells and small animals. *Nat. Protoc.* **2013**, *8*, 2033-2044.

[58] Joubert, M.-F. Photon avalanche upconversion in rare earth laser materials. *Opt. Mater.* **1999**, *11*, 181-203.

[59] Wang, F.; Banerjee, D.; Liu, Y.; Chen, X.; Liu, X. Upconversion nanoparticles in biological labeling, imaging, and therapy. *Analyst* **2010**, *135*, 1839-1854.

[60] Cheng, L.; Wang, C.; Liu, Z. Upconversion nanoparticles and their composite nanostructures for biomedical imaging and cancer therapy. *Nanoscale* **2013**, *5*, 23-37.

[61] Park, Y. I.; Lee, K. T.; Suh, Y. D.; Hyeon, T. Upconverting nanoparticles: a versatile platform for wide-field two-photon microscopy and multi-modal in vivo imaging. *Chem. Soc. Rev.* **2015**, *44*, 1302-1317.

[62] Zhou, J.; Liu, Q.; Feng, W.; Sun, Y.; Li, F. Upconversion luminescent materials: advances and applications. *Chem. Rev.* **2014**, *115*, 395-465.

[63] Chen, G.; Ågren, H.; Ohulchanskyy, T. Y.; Prasad, P. N. Light upconverting core–shell nanostructures: nanophotonic control for emerging applications. *Chem. Soc. Rev.* **2015**, *44*, 1680-1713.

[64] Li, X.; Zhang, F.; Zhao, D. Lab on upconversion nanoparticles: optical properties and applications engineering via designed nanostructure. *Chem. Soc. Rev.* **2015**, *44*, 1346-1378.

[65] Liu, X.; Deng, R.; Zhang, Y.; Wang, Y.; Chang, H.; Huang, L.; Liu, X. Probing the nature of upconversion nanocrystals: instrumentation matters. *Chem. Soc. Rev.* **2015**, *44*, 1479-1508.

[66] Dong, H.; Sun, L.-D.; Yan, C.-H. Energy transfer in lanthanide upconversion studies for extended optical applications. *Chem. Soc. Rev.* **2015**, *44*, 1608-1634.

[67] Peng, J.; Xu, W.; Teoh, C. L.; Han, S.; Kim, B.; Samanta, A.; Er, J. C.; Wang, L.; Yuan, L.; Liu, X.; Chang, Y.-T. High-efficiency in vitro and in vivo detection of Zn2+ by dye-assembled upconversion nanoparticles. *J. Am. Chem. Soc.* **2015**, *137*, 2336-2342.

[68] Chen, Z.; Liu, Z.; Li, Z.; Ju, E.; Gao, N.; Zhou, L.; Ren, J.; Qu, X. Upconversion nanoprobes for efficiently in vitro imaging reactive oxygen species and in vivo diagnosing rheumatoid arthritis. *Biomaterials* **2015**, *39*, 15-22.

[69] Fan, W.; Bu, W.; Shen, B.; He, Q.; Cui, Z.; Liu, Y.; Zheng, X.; Zhao, K.; Shi, J. Intelligent MnO2 Nanosheets Anchored

with Upconversion Nanoprobes for Concurrent pH-/H_2O_2-Responsive UCL Imaging and Oxygen-Elevated Synergetic Therapy. *Adv. Mater.* **2015**, *27*, 4155-4161.

[70] Li, Z.; Liang, T.; Lv, S.; Zhuang, Q.; Liu, Z. A rationally designed upconversion nanoprobe for in vivo detection of hydroxyl radical. *J. Am. Chem. Soc.* **2015**, *137*, 11179-11185.

[71] Peng, J.; Samanta, A.; Zeng, X.; Han, S.; Wang, L.; Su, D.; Loong, D. T. B.; Kang, N. Y.; Park, S. J.; All, A. H.; Jiang, W.; Lin, Y.; Liu, X.; Chang, Y.-T. Real-Time In Vivo Hepatotoxicity Monitoring through Chromophore-Conjugated Photon-Upconverting Nanoprobes. *Angew. Chem. Int. Edit.* **2017**, *56*, 4165-4169.

[72] Seo, Y. H.; Singh, A.; Cho, H.-J.; Kim, Y.; Heo, J.; Lim, C.-K.; Park, S. Y.; Jang, W.-D.; Kim, S. Rational design for enhancing inflammation-responsive in vivo chemiluminescence via nanophotonic energy relay to near-infrared AIE-active conjugated polymer. *Biomaterials* **2016**, *84*, 111-118.

[73] Mao, D.; Wu, W.; Ji, S.; Chen, C.; Hu, F.; Kong, D.; Ding, D.; Liu, B. Chemiluminescence-guided cancer therapy using a chemiexcited photosensitizer. *Chem* **2017**, *3*, 991-1007.

[74] Lim, C. K.; Lee, Y. D.; Na, J.; Oh, J. M.; Her, S.; Kim, K.; Choi, K.; Kim, S.; Kwon, I. C. Chemiluminescence-generating nanoreactor formulation for near-infrared imaging of hydrogen peroxide and glucose level in vivo. *Adv. Funct. Mater.* **2010**, *20*, 2644-2648.

[75] Lee, D.; Khaja, S.; Velasquez-Castano, J. C.; Dasari, M.; Sun, C.; Petros, J.; Taylor, W. R.; Murthy, N. In vivo imaging of hydrogen peroxide with chemiluminescent nanoparticles. *Nat. Mater.* **2007**, *6*, 765-769.

[76] Cho, S.; Hwang, O.; Lee, I.; Lee, G.; Yoo, D.; Khang, G.; Kang, P. M.; Lee, D. Chemiluminescent and antioxidant micelles as theranostic agents for hydrogen peroxide associated-inflammatory diseases. *Adv. Funct. Mater.* **2012**, *22*, 4038-4043.

[77] Shuhendler, A. J.; Pu, K.; Cui, L.; Uetrecht, J. P.; Rao, J. Real-time imaging of oxidative and nitrosative stress in the liver of live animals for drug-toxicity testing. *Nat. Biotechnol.* **2014**, *32*, 373.

[78] Zhen, X.; Zhang, C.; Xie, C.; Miao, Q.; Lim, K. L.; Pu, K. Intraparticle energy level alignment of semiconducting polymer nanoparticles to amplify chemiluminescence for ultrasensitive in vivo imaging of reactive oxygen species. *ACS Nano* **2016**, *10*, 6400-6409.

[79] Lee, Y.-D.; Lim, C.-K.; Singh, A.; Koh, J.; Kim, J.; Kwon, I. C.; Kim, S. Dye/peroxalate aggregated nanoparticles with enhanced and tunable chemiluminescence for biomedical imaging of hydrogen peroxide. *ACS Nano* **2012**, *6*, 6759-6766.

[80] Yu, J.; Rong, Y.; Kuo, C.-T.; Zhou, X.-H.; Chiu, D. T. Recent advances in the development of highly luminescent semiconducting polymer dots and nanoparticles for biological imaging and medicine. *Anal. Chem.* **2016**, *89*, 42-56.

[81] Wang, J.; Lv, F.; Liu, L.; Ma, Y.; Wang, S. Strategies to design conjugated polymer based materials for biological sensing and imaging. *Coordin. Chem. Rev.* **2017**.

[82] Nishihara, R.; Suzuki, H.; Hoshino, E.; Suganuma, S.; Sato, M.; Saitoh, T.; Nishiyama, S.; Iwasawa, N.; Citterio, D.; Suzuki, K. Bioluminescent coelenterazine derivatives with imidazopyrazinone C-6 extended substitution. *Chem. Commun.* **2014**, *51*, 391-394.

[83] Li, P.; Liu, L.; Xiao, H.; Zhang, W.; Wang, L.; Tang, B. A new polymer nanoprobe based on chemiluminescence resonance energy transfer for ultrasensitive imaging of intrinsic superoxide anion in mice. *J. Am. Chem. Soc.* **2016**, *138*, 2893-2896.

[84] Choi, H. S.; Gibbs, S. L.; Lee, J. H.; Kim, S. H.; Ashitate, Y.; Liu, F.; Hyun, H.; Park, G.; Xie, Y.; Bae, S.; Henary, M.; Frangioni, J. V. Targeted zwitterionic near-infrared fluorophores for improved optical imaging. *Nat. Biotechnol.* **2013**, *31*, 148-153.

[85] Hong, G.; Lee, J. C.; Robinson, J. T.; Raaz, U.; Xie, L.; Huang, N. F.; Cooke, J. P.; Dai, H. Multifunctional in vivo vascular imaging using near-infrared II fluorescence. *Nat. Med.* **2012**, *18*, 1841-1846.

[86] Wang, L. V.; Hu, S. Photoacoustic tomography: in vivo imaging from organelles to organs. *Science* **2012**, *335*, 1458-1462.

[87] Weber, J.; Beard, P. C.; Bohndiek, S. E. Contrast agents for molecular photoacoustic imaging. *Nat. Methods* **2016**, *13*, 639-650.

[88] Kim, C.; Favazza, C.; Wang, L. V. In vivo photoacoustic tomography of chemicals: high-resolution functional and molecular optical imaging at new depths. *Chem. Rev.* **2010**, *110*, 2756-2782.

[89] Xu, M.; Wang, L. V. Photoacoustic imaging in biomedicine. *Rev. Sci. Instrum.* **2006**, *77*, 041101.

[90] Zerda, A. d. l.; Zavaleta, C.; Keren, S.; Vaithilingam, S.; Bodapati, S.; Liu, Z.; Levi, J.; Smith, B. R.; Ma, T.-J.; Oralkan, O.; Cheng, Z.; Chen, X.; Dai, H.; Khuri-Yakub, B. T.; Gambhir, S. S. Carbon nanotubes as photoacoustic molecular imaging agents in living mice. *Nat. Nanotechnol.* **2008**, *3*, 557-562.

[91] Zerda, A. d. l.; Liu, Z.; Bodapati, S.; Teed, R.; Vaithilingam, S.; Khuri-Yakub, B. T.; Chen, X.; Dai, H.; Gambhir, S. S. Ultrahigh sensitivity carbon nanotube agents for photoacoustic molecular imaging in living mice. *Nano Lett.* **2010**, *10*, 2168-2172.

[92] Fan, Q.; Cheng, K.; Yang, Z.; Zhang, R.; Yang, M.; Hu, X.; Ma, X.; Bu, L.; Lu, X.; Xiong, X.; Huang, W.; Zhao, H.; Cheng, Z. Perylene-Diimide-Based Nanoparticles as Highly Efficient Photoacoustic Agents for Deep Brain Tumor Imaging in Living Mice. *Adv. Mater.* **2015**, *27*, 843-847.

[93] Wang, J.; Chen, F.; Arconada-Alvarez, S. J.; Hartanto, J.; Yap, L.-P.; Park, R.; Wang, F.; Vorobyova, I.; Dagliyan, G.; Conti, P. S.; Jokerst, J. V. A Nanoscale Tool for

Photoacoustic-based Measurements of Clotting Time and Therapeutic Drug Monitoring of Heparin. *Nano Lett.* **2016**, *16*, 6265-6271.

[94] Zhen, X.; Zhang, J.; Huang, J.; Xie, C.; Miao, Q.; Pu, K. Macrotheranostic Probe with Disease-activated Near-infrared Fluorescence, Photoacoustic and Photothermal Signals for Imaging-guided Therapy. *Angew. Chem. Int. Edit.* **2018**, DOI: 10.1002/anie. 201803321.

[95] Chen, M.; Tang, S.; Guo, Z.; Wang, X.; Mo, S.; Huang, X.; Liu, G.; Zheng, N. Core–Shell Pd@ Au Nanoplates as Theranostic Agents for In-Vivo Photoacoustic Imaging, CT Imaging, and Photothermal Therapy. *Adv. Mater.* **2014**, *26*, 8210-8216.

[96] Yang, K.; Hu, L.; Ma, X.; Ye, S.; Cheng, L.; Shi, X.; Li, C.; Li, Y.; Liu, Z. Multimodal imaging guided photothermal therapy using functionalized graphene nanosheets anchored with magnetic nanoparticles. *Adv. Mater.* **2012**, *24*, 1868-1872.

[97] Lovell, J. F.; Jin, C. S.; Huynh, E.; Jin, H.; Kim, C.; Rubinstein, J. L.; Chan, W. C.; Cao, W.;Wang, L. V.; Zheng, G. Porphysome nanovesicles generated by porphyrin bilayers for use as multimodal biophotonic contrast agents. *Nat. Mater.* **2011**, *10*, 324-332.

[98] Lyu, Y.; Fang, Y.; Miao, Q.; Zhen, X.; Ding, D.; Pu, K. Intraparticle molecular orbital engineering of semiconducting polymer nanoparticles as amplified theranostics for in vivo photoacoustic imaging and photothermal therapy. *ACS Nano* **2016**, *10*, 4472-4481.

[99] Zhen, X.; Xie, C.; Jiang, Y.; Ai, X.; Xing, B.; Pu, K. Semiconducting Photothermal Nanoagonist for Remote-controlled Specific Cancer Therapy. *Nano Lett.* **2018**, *18*, 1498-1505.

[100] Xie, C.; Cheng, P.; Pu, K. Synthesis of PEGylated Semiconducting Polymer Amphiphiles for Molecular Photoacoustic Imaging and Guided Therapy. *Chem.-Eur. J.* **2018**, 201705716.

[101] Jiang, Y.; Pu, K. Advanced Photoacoustic Imaging Applications of Near-Infrared Absorbing Organic Nanoparticles. *Small* **2017**, *13*, 1700710.

[102] Cui, D.; Xie, C.; Pu, K. Development of semiconducting polymer nanoparticles for photoacoustic imaging. *Macromol. Rapid Comm.* **2017**, *38*, 1700125.

[103] Lovell, J. F.; Liu, T. W.; Chen, J.; Zheng, G. Activatable photosensitizers for imaging and therapy. *Chem. Rev.* **2010**, *110*, 2839-2857.

[104] Miao, Q.; Pu, K. Emerging Designs of activatable photoacoustic probes for molecular imaging. *Bioconjugate Chem.* **2016**, *27*, 2808-2823.

[105] Pu, K.; Shuhendler, A. J.; Jokerst, J. V.; Mei, J.; Gambhir, S. S.; Bao, Z.; Rao, J. Semiconducting polymer nanoparticles as photoacoustic molecular imaging probes in living mice. *Nat. Nanotechnol.* **2014**, *9*, 233-239.

[106] Yin, C.; Zhen, X.; Fan, Q.; Huang, W.; Pu, K. Degradable semiconducting oligomer amphiphile for ratiometric photoacoustic imaging of hypochlorite. *ACS Nano* **2017**, *11*, 4174-4182.

[107] Zhang, J.; Zhen, X.; Upputuri, P. K.; Pramanik, M.; Chen, P.; Pu, K. Activatable photoacoustic nanoprobes for in vivo ratiometric imaging of peroxynitrite. *Adv. Mater.* **2017**, *29*, 1604764.

[108] Chen, Q.; Liang, C.; Sun, X.; Chen, J.; Yang, Z.; Zhao, H.; Feng, L.; Liu, Z. H_2O_2-responsive liposomal nanoprobe for photoacoustic inflammation imaging and tumor theranostics via in vivo chromogenic assay. *P. Natl. Acad. Sci. USA* **2017**, *114*, 5343-5348.

[109] Xie, C.; Zhen, X.; Lyu, Y.; Pu, K. Nanoparticle Regrowth Enhances Photoacoustic Signals of Semiconducting Macromolecular Probe for In Vivo Imaging. *Adv. Mater.* **2017**, *29*, 1703693.

[110] Huryn, D. M.; Resnick, L. O.; Wipf, P. Contributions of Academic Laboratories to the Discovery and Development of Chemical Biology Tools: Miniperspective. *J. Med. Chem.* **2013**, *56*, 7161-7176.

[111] Li, L. L.; Ma, H. L.; Qi, G. B.; Zhang, D.; Yu, F.; Hu, Z.; Wang, H. Pathological-Condition-Driven Construction of Supramolecular Nanoassemblies for Bacterial Infection Detection. *Adv. Mater.* **2016**, *28*, 254-262.

[112] Zhen, X.; Feng, X.; Xie, C.; Zheng, Y.; Pu, K. Surface engineering of semiconducting polymer nanoparticles for amplified photoacoustic imaging. *Biomaterials* **2017**, *127*, 97-106.

[113] Cremer, J. W.; Covert, P. A.; Parmentier, E. A.; Signorell, R. Direct measurement of photoacoustic signal sensitivity to aerosol particle size. *J. Phys. Chem. Lett.* **2017**, *8*, 3398-3403.

[114] Jiang, Y.; Pu, K. Molecular Fluorescence and Photoacoustic Imaging in the Second Near-Infrared Optical Window Using Organic Contrast Agents. *Adv. Biosyst.* **2018**, 1700262.